# TURBULENT RECIRCULATING FLOW

# WITHIN A CAVITY

AN EXPERIMENTAL AND NUMERICAL

INVESTIGATION OF TURBULENT RECIRCULATING

FLOW WITHIN A CAVITY WITH AN INLET WALL JET

DAVID ANDREW JOHNSON

B. Eng. (McMaster)

A Thesis
Submitted to the School of Graduate Studies
in Partial Fulfillment of the Requirements
for the Degree
Master of Engineering

McMaster University
September 1988

TO MY PARENTS

MASTER OF ENGINEERING (1988)   McMaster University
(Mechanical Engineering)        Hamilton, Ontario

TITLE:    An Experimental and Numerical Investigation of
          Turbulent Recirculating Flow within a Cavity
          with an Inlet Wall Jet

AUTHOR:   David Andrew Johnson,            ← you suck at writing!
          B.Eng. (McMaster University)

SUPERVISOR:    Professor M. Shoukri

NUMBER OF PAGES:    xiii, 130

ABSTRACT

Recirculating turbulent flow within a cavity with an inlet wall jet was examined. In steady water flow velocity profiles were constructed with measurements taken with a Laser Doppler Anemometer system mounted on a traversing mechanism. Two test cases were examined Re jet = 1167 and Re jet = 3231 as well as developing wall jet profiles.

The results are presented with mean velocity plots and turbulent kinetic energy contours. Comparisons are then made with results obtained using a finite difference computational scheme based on the $k - \epsilon$ turbulence model. Good agreement was obtained between the computer code predictions and the experimental data.

## ACKNOWLEDGEMENTS

v

# TABLE OF CONTENTS

## NOMENCLATURE

| | |
|---|---|
| $C_1$ | Empirical turbulence model constant |
| $C_2$ | Empirical turbulence model constant |
| $C_3$ | Empirical turbulence model constant |
| $C_\mu$ | Empirical turbulence model constant |
| $d_f$ | fringe spacing |
| $k$ | Turbulent kinetic energy |
| $\kappa$ | Von Karman's constant |
| $l$ | length scale of turbulence |
| $l_m$ | mixing length |
| $L$ | width of jet mouth |
| $P$ | mean pressure |
| $p'$ | fluctuating pressure |
| $p$ | instantaneous pressure |
| $t, \theta$ | time |
| $\Delta t$ | time step |
| $u$ | instantaneous velocity component in x direction |
| $U$ | mean velocity component in x direction |
| $u'$ | fluctuating velocity in x direction |
| $v$ | instantaneous velocity component in y direction |
| $V$ | mean velocity component in y direction |
| $v'$ | fluctuating velocity in y direction |

| | |
|---|---|
| w | instantaneous velocity component in z direction |
| W | mean velocity component in z direction |
| w' | fluctuating velocity in z direction |
| x,y,z | coordinate directions |
| $\Delta$x | grid spacing in x direction |
| $\Delta$y | grid spacing in y direction |
| | |
| $\epsilon$ | dissipation rate of turbulent kinetic energy |
| $\mu$ | viscosity |
| $\rho$ | density |
| $\sigma_k$ | Prandtl-Schmidt number for turbulent kinetic energy |
| $\sigma_\epsilon$ | Prandtl-Schmidt number for dissipation rate |
| $\sigma_t$ | Turbulent Prandtl number |
| $\sigma_x$ | width of measurement volume |
| $\tau$ | Shear stress |

## Subscripts

| | |
|---|---|
| e | effective |
| i,j | vector directions i,j |
| w | wall |

# LIST OF FIGURES

CHAPTER ONE

INTRODUCTION


Turbulent recirculating flow occurs in many areas
of engineering interest including environmental studies,
ventilation, and power generation.  Simulations of
turbulent fluid dynamics have become increasingly
important in recent years in the above areas in order to
predict flow patterns and velocity profiles.

The main motivation for examining turbulent
recirculating flow in a cavity was to provide
experimental data with which to compare and verify
numerical simulations of two dimensional isothermal
turbulent flows.  Numerical simulations were performed
using a finite difference solution of the conservation
equations in which turbulence is modelled by a two
equation turbulence model.

The two equation $k - \epsilon$ turbulence model is widely
used for such applications although very little
experimental work on recirculating flows has been done
to verify such models.

In the present case the recirculating flow cavity
was  constructed to simulate a two dimensional cavity.
Flow entered the cavity by means of an inlet wall jet

and the entry area is examined in some detail. The experimental results were then used to verify the $k - \epsilon$ model used.

# CHAPTER TWO

## LITERATURE REVIEW

### 2.1 TURBULENCE MODELLING

An overview of turbulence modelling is presented as
well as the origins of the turbulence parameters from
the constitutive equations.  Numerous modelling methods
are discussed with reference to specific proposed
models.  The presentation is far from comprehensive but
details the current directions in turbulence modelling.
For closure, possible future directions and models are
discussed.

### 2.1.1 Introduction

Turbulence is a common phenomena in fluid analysis
and is much more frequent than the predictable laminar
flow which has been documented extensively.

Turbulence can be characterized by random
fluctuations in fluid parameters with time in both
magnitude and direction (vectors).  It generally has
high dissipation rates, is diffuse while at the same
time is continuous and obeys all the conservation laws.
Some definitions will now be given to aid in char-

acterizing turbulent flow.

Defining a mean velocity in the x direction

$$U = \frac{1}{t} \int_0^t u_x \, d\theta \tag{2.1.1}$$

where $\theta$ is the time

If mean quantities are found to be constant then the turbulence is at steady state with respect to the mean flow.

Instantaneous variables are defined and are the sum of mean and fluctuating components.

$$u = U + u' \tag{2.1.2}$$

$$\overline{u'} = \frac{1}{t} \int_0^t u'_x \, d\theta = 0 \tag{2.1.3}$$

Intensity of turbulence

$$I = \frac{\sqrt{\frac{1}{3}(\overline{u'^2} + \overline{v'^2} + \overline{w'^2})}}{U} \tag{2.1.4}$$

If the Navier Stokes equations are now detailed for steady isothermal Newtonian flow in cartesian coordinates for the instantaneous variables they become:

Continuity

$$\frac{\partial (u_i)}{\partial x_i} = 0$$

(2.1.5)

Momentum

$$u_j \frac{\partial (u_i)}{\partial x_j} = \frac{-1}{\rho} \frac{\partial p_i}{\partial x_i} + \frac{\mu}{\rho} \left( \frac{\partial^2 u_i}{\partial x_j^2} \right)$$

(2.1.6)

All flows are subject to the conservation laws and can be described using the field equations for the conservation of mass, momentum and energy. In addition to these laws, various constitutive relations are required to close the set of conservation equations. The only criterion for application of the laws of conservation in the integral balance form is that the media being conserved is continuous.

In all fluid flows some randomness can be expected

due to many factors including surface effects or energy input and it is for this reason that averaging is required. With the proper use of averaging, properties of the fluid may be determined and field and constitutive equations may be found.

In turbulent single phase flows, flow prediction is very difficult due to the random fluctuating components of flow parameters such as velocity, pressure, and temperature. Individual fluctuating components are measurable but are of no use for engineering purposes due to their time and spatial dependence.

For the above reasons, averaging procedures are performed in order to predict flow parameters, and flow behaviour in fluctuating flow fields.

The method used to transform the local instantaneous properties to usable information is averaging. Proper averaging should result in mean values of flow parameters which describe its macroscopic behaviour and are measurable as well. Mathematically, mean flow parameters must be continuous and have continuous first derivatives. Eulerian averaging uses the time-space description of events in integral forms which is ideal for the flows being discussed. Averaging over time and space in effect smooths out any local variations in the flow field.

The time average method is used in turbulent single phase flows. For single phase time averaged turbulent flows the local instantaneous variable (velocity, for example) is transformed into two components; a time - smoothed component and a fluctuating component. These components then replace the instantaneous variable in the conservation field equations and Eulerian time averaging is performed. Obviously, the average of the fluctuating component is zero as it fluctuates about the time-smoothed component only. When this procedure is performed additional terms arise which are called the turbulent momentum flux or Reynolds stresses. Attempts have been made to describe these stresses empirically depending on flow geometry and flow pattern.

In time averaging single phase turbulent flow aspects of the flow pattern can be lost. For example, time averaging depends on the length of time over which the averaging is performed. If a large sampling time is taken significant flow profiles could be lost while a short time average could lead to a fluctuating average component. The range of randomness in the flow or intensity of turbulence is usually lost in the time average. The range could be important for design of equipment or for maximum and minimum expected values.

Averaging techniques are widely used in evaluating

flow parameters of engineering interest. Although significant flow information can be lost when quantities are averaged, external relationships and correlation coefficients can account for some of the missing information. With the proper selection of an averaging technique and the proper time step and/or area average reliable results can be predicted [1]. The instantaneous variables will now be transformed into the sum of the mean and fluctuating components and these values will be substituted into the conservation equations.

Continuity

$$\frac{\partial (U_i + u'_i)}{\partial x_i} = 0 \qquad (2.1.7)$$

Momentum

$$(U_j + u'_j) \frac{\partial (U_j + u'_j)}{\partial x_j} = -\frac{1}{\rho} \frac{\partial (P_i + p'_i)}{\partial x_i}$$

$$+ \frac{\mu}{\rho} \left[ \frac{\partial^2 (U_j + u'_j)}{\partial x_j^2} \right] \qquad (2.1.8)$$

Averaging over time gives

Continuity

$$\frac{\partial (U_i)}{\partial x_i} = 0 \qquad (2.1.9)$$

Momentum (x direction)

$$\frac{\partial (U^2)}{\partial x} + \frac{\partial (\overline{u'})^2}{\partial x} + \frac{\partial (UV)}{\partial y} + \frac{\partial (\overline{u'v'})}{\partial y} + \frac{\partial (UW)}{\partial z} + \frac{\partial (\overline{u'w'})}{\partial z} = \qquad (2.1.10)$$

$$\frac{-1}{\rho} \frac{\partial P}{\partial x} + \frac{\mu}{\rho} \left[ \frac{\partial^2 U}{\partial x^2} + \frac{\partial^2 U}{\partial y^2} + \frac{\partial^2 U}{\partial z^2} \right]$$

Utilizing the continuity equations the momentum equation in the x direction can be written as

$$\frac{U\partial (U)}{\partial x} + \frac{V\partial (U)}{\partial y} + \frac{W\partial (U)}{\partial z} = \frac{-1}{\rho} \frac{\partial P}{\partial x} + \frac{\mu}{\rho} \left[ \frac{\partial^2 U}{\partial x^2} + \frac{\partial^2 V}{\partial y^2} + \frac{\partial^2 W}{\partial z^2} \right]$$

$$- \frac{\partial (\overline{u'})^2}{\partial x} - \frac{\partial (\overline{u'v'})}{\partial y} - \frac{\partial (\overline{u'w'})}{\partial z} \qquad (2.1.11)$$

Similar equations can be written in the y and z directions.

The only terms which differ from the instantaneous equations are the Reynolds stresses or turbulent momentum flux $\overline{u_i' u_j'}$ (the cross correlation of the fluctuating quantities). There are now more unknown quantities than equations and solution is not possible until the Reynolds stress terms are further defined. These stresses are difficult to evaluate in their present form and proposals to model them are discussed later.

## 2.1.2 Modelling Proposals

A useful turbulence model will be applicable to a large number of flows with accuracy, be fairly simple to apply or to have only those complications which would greatly increase its accuracy or applicability.

As an effort to define the turbulent stress components in 1877 Boussinesq [2] expressed the stress in terms of mean flow parameters

$$\tau_{ij} = -\rho \overline{u_i' u_j'} = \mu_t \left( \frac{\partial U_i}{\partial x_j} + \frac{\partial U_j}{\partial x_i} \right) - \frac{2}{3} \rho k \delta_{ij} \qquad (2.1.12)$$

The turbulent viscosity $\mu_t$ , not a property of the fluid, is dependant on the local turbulent flow structure and is predicted using many models.  A model which is based on an algebraic equation will be discussed first.

i) Algebraic formulae for $\mu_t$

The first proposal was Prandtl's mixing length hypothesis which is in two parts and was proposed in 1925 by Prandtl [3].

1.     $\mu_t = \rho l_m V_t$ (2.1.13)

2.     $V_t = l_m \dfrac{dU}{dy}$ (2.1.14)

where $v_t$ is a velocity scale and $l_m$ is the mixing length

The mixing length is the unknown in Prandtl's hypothesis and it is a function of position.    Prandtl proposed

$$l_m \propto y$$ (2.1.15)

where y is the distance to the nearest wall.

The mixing length hypothesis is simple to use, requires no solution of differential equations and with the proper choice of mixing length good predictions can be made.   Many researchers have used the mixing length and data is available.   The model has numerous drawbacks such as it cannot predict recirculating flows as the relationships between stress and velocity gradients are too complicated, and it implies that the turbulent viscosity disappears when the velocity gradient is zero. Also, it does not account for the process of convection or diffusion of turbulence.

In summary then, the mixing length hypothesis as an example of an algebraic equation for turbulent viscosity is useful for simple shear layers as the mixing length distribution can be specified empirically [4].

ii) One equation models of turbulence

In order to satisfy some of the drawbacks of the algebraic formula for $\mu_t$ differential transport equations were proposed for the transport of turbulent quantities. An advantage is that the fluctuating velocity scale is now determined from a transport equation and is no longer linked to the mean velocity gradients. The first were proposed by Kolmogorov (1942) [5] and Prandtl (1945) [6] who proposed

$$\mu_t = \rho l \sqrt{k} \qquad (2.1.16)$$

where l is a length scale and k is the time averaged turbulence kinetic energy defined as

$$k = \frac{1}{2} \left[ \overline{u'}^2 + \overline{v'}^2 + \overline{w'}^2 \right] \qquad (2.1.17)$$

A model transport equation for k can be derived from the Navier - Stokes equations [7].

$$\frac{\partial (kU_i)}{\partial x_i} = \frac{\partial}{\partial x_i} \left[ \frac{\mu_e}{\rho \sigma_k} \frac{\partial k}{\partial x_i} \right] + \frac{\mu_t}{\rho} \left[ \frac{\partial U_i}{\partial x_j} + \frac{\partial U_j}{\partial x_i} \right] \frac{\partial U_i}{\partial x_j} - \epsilon$$

(i)             (ii)                 (iii)               (iv)

(2.1.18)

Each term may be interpreted as follows:

i)    This is the convective transport of kinetic energy
      due to the mean flow.

ii)   This is the diffusive transport of kinetic energy
      due to velocity and pressure fluctuations.

iii)  This is the generation of kinetic energy by the
      interaction of turbulent stresses and mean velocity
      gradients.

iv)   This term is the dissipation of kinetic energy by
      viscous action.

These energy models using the kinetic energy term
are difficult to use as l must still be empirically
predicted.

For the one equation models $k^{1/2}$ is a better
turbulent velocity scale than $l_m \frac{dU}{dy}$ . Recirculating
flows can not be predicted with one equation and some
form of turbulent length should be included.

iii) Two equation models of turbulence

In order to overcome the problems with both the length scale method (mixing length) and the energy scale method (kinetic energy) a method was developed combining both a length scale and an energy scale in the transport equations. The proposed approach is to use a variable which combines both the turbulent energy scale and the length scale. The new parameter is given by

$$Z = k^m \, l^n \qquad\qquad (2.1.19)$$

Two differential equations for the transport of k and Z must now be solved. Numerous models have been proposed using this method and a summary is shown in Table 1 [8]. The most widely used variable is the dissipation rate of turbulent kinetic energy $\epsilon$ and the model is accordingly called the k - $\epsilon$ model. It was proposed by Chou (1945) [9] and others (see Table 1).

$$(2.1.20)$$

$$\epsilon = \frac{k^{3/2}}{l}$$

| Proposer, Year | Z | Symbol |
|---|---|---|
| Kolmogorov (1942) | $k^{1/2}/l$ | f |
| Chou (1945), Davidov (1961) Jones–Launder (1972) | $k^{3/2}/l$ | $\epsilon$ |
| Rotta (1951) Spalding (1967b) | $l$ | $l$ |
| Rotta (1968,1971) Rodi–Spalding (1970) | $kl$ | $kl$ |
| Spalding (1969) | $k/l^2$ | W |

from Mathematical Models of Turbulence
B. Launder and D. Spalding
1972 Academic Press

# Table 1

# Some proposals for Z

A **model** transport equation for $\epsilon$ can be derived from the Navier - Stokes equations [7].

$$\frac{\partial}{\partial x_i}(\epsilon U_i) = \frac{\partial}{\partial x_i}\left[\frac{\mu_e}{\rho\sigma_e}\frac{\partial\epsilon}{\partial x_i}\right]$$

$$+ C_1\frac{\epsilon}{k}\frac{\mu_t}{\rho}\left[\frac{\partial U_i}{\partial x_j} + \frac{\partial U_j}{\partial x_i}\right]\frac{\partial U_i}{\partial x_j} - C_2\frac{\epsilon^2}{k} \tag{2.1.21}$$

The model relates the turbulent kinetic energy k and dissipation rate $\epsilon$ to the turbulent viscosity $\mu_t$ by

$$\mu_t = C_\mu\,\rho\,\frac{k^2}{\epsilon} \tag{2.1.22}$$

The effective viscosity is then

$$\mu_e = \mu_t + \mu \tag{2.1.23}$$

The k - $\epsilon$ model is suitable for fairly complex flows and has been tested for a wide range of problems. It is the simplest model that will predict recirculating flows. It is a fairly universal model just the constants must be determined.

iv) Multi equation models of turbulence

These models are fairly complex and simulate turbulence realistically. They are based on the turbulent stresses themselves not on a turbulent viscosity. Constants must still be determined depending on geometry, etc. These models are called stress/flux models and are not generally applicable. For examples see Chou [9] and others.

v) Statistical Theories of Turbulence

These theories are mathematically oriented and are based on probability concepts. The basis of these theories comes from the random nature of turbulence. Examples of statistical theories would be Kolmogoroff and Heisenberg [10].

## 2.1.3 Future Developments

The direction turbulence modelling could take will be towards more complex models with the desire of the modeler to model the fundamental reasons for turbulence. There will be some attempt to predict turbulence through the size of eddies or through the development of the energy exchange from larger eddies to smaller eddies. Other future work could be in the area of refining the present models, making them more comprehensive and widening their applications.

## 2.2 RECIRCULATING FLOW

Very little experimental work has been done for the case of recirculating flow within a cavity. Some papers on the more general topic of recirculating flow will be examined. The majority of the investigations involving recirculating flow have been in the area of recirculation past a step change or sudden expansion. These studies are in some aspects similar to the present case study and several papers will be examined.

Baron, Benque, and Coeffe [11] have examined the case of three dimensional turbulent flow caused by a jet entering a cavity. The cubic cavity (50 cm side) had two horizontal windows for flow entry and exit. The windows were not symmetrically placed such that the jet entering the cavity would impinge on the opposing wall before exiting the cavity. The measurements in the cavity were obtained using a two component laser doppler anemometer. Flow patterns were presented and comparisons were made with a numerical computation scheme based on the solution of the non stationary Navier Stokes equations for large scale three dimensional incompressible fluid flow. The method involved a time advancing finite difference scheme using two staggered grids.

The code was able to predict the main aspects of the flow in the velocity profiles but was unable to reproduce the turbulent energy profiles. In particular it was unable to predict the increase in turbulent energy from the entrance to the inside of the box.

Tanaka et al [12] have examined primarily the temperature effects in a 1/10 scale model of a Liquid Metal Fast Breeder Reactor (LMFBR) hot plenum in both transient and steady state operation. The velocity profiles were obtained using a propeller velocimeter using a 9 X 15 measurement grid. The test tank was a cylindrical vessel with a variable height intake and discharge. Results were shown for various combinations of intake and discharge. For comparison a numerical solution was generated using a forward time finite difference scheme. This method gave good predictions of the bulk flow with the exception of poor agreement for the case of a high discharge and a low intake. Turbulent kinetic energy profiles were not obtained in this study.

A comparison of numerical and experimental work was done by Ushijima et al [13] on a rectangular plenum (52 X 45 X 5 cm). Using a 21 X 5 grid (spacing 10 cm horizontally and 2.5 cm vertically) measurements of steady, isothermal water flow were taken using a He Ne

LDA system.   For comparison with experimental results three turbulence models were used.   They were the k-$\epsilon$ model, the Launder Reynolds stress model (LRSM), and the Simplified Reynolds stress model (SRSM) all using two dimensional conditions.

The method of finite differences was used with a staggered mesh and all variables except velocity were cell centred and velocity located on the cell boundary.

The numerical models gave a good prediction of the bulk flow present with the exception of the top of the rectangular plenum where poor agreement was obtained due to three dimensional effects and corner boundary conditions.   The normal stresses $\overline{u'}^2$   and $\overline{v'}^2$ were predicted poorly by all the models used.

Boyle and Golay [14] have examined a 1/15 (15.24 X 22.86 X 6.08 cm) scale model of the Fast Flux Test Facility (FFTF) reactor outlet plenum.   The rectangular model studied had a  vertical inlet (2.86 cm wide) near the bottom and a horizontal outlet (1.91 cm wide) also at the bottom of the model.   The cavity was considered two dimensional and the measurements were made mid-plane of the symmetrical z axis (depth 6.08 cm).   Measurements of velocity and kinetic energy were obtained using a two channel Laser Doppler Anemometer at 79 regularly spaced points in the tank.   Comparisons were made using the

computer code VARR-II which solves the incompressible mean flow Navier Stokes equations in two dimensions. The turbulence model used in this study was the $k - \sigma$ turbulence model of Stuhmiller although the more common $k - \epsilon$ model was also used with the TEACH-T code. Using a 16 X 24 computational grid good agreement with the bulk flow was observed with the exception of the upper portion of the tank where it was believed three dimensional effects ocurred due to the jet impinging on the top of the tank. The velocity gradient at the wall was not predicted well with the code and this was probably due to too coarse a computational grid. The turbulent kinetic energy computed did not agree well with the experimental results in value or in profiles.

In a continuation of the work [15] transient flow cases were examined and compared to turbulence model predictions.

Studies of recirculation as a result of a step change or sudden expansion are comparable in some respects to the present study and some of these will be examined now.

A rectangular rearward facing step and a cylindrical sudden expansion were examined by Thompson, Stevenson and Craig [16]. Measurements were obtained with a Laser Doppler Anemometer mounted on a traversing

mechanism. Reasonable agreement with the CHAMPION 2/E/FIX computer code using the k - $\epsilon$ turbulence model on a 41 X 41 computational grid was obtained. A 21 X 21 grid was found suitable for bulk flow predictions but a 41 X 41 grid was required for kinetic energy predictions. Even with the 41 X 41 grid poor agreement with the measured turbulent kinetic energy was obtained.

Similarly, Moss, Baker and Bradbury [17] have used a pulsed wire anemometer to investigate a flat plate, a backward facing step, and a forward facing step. The size of the measurement probe did not allow full examination of the recirculating area and the hot wire anemometer was not recommended for such highly turbulent flows. No computer predictions were presented as the investigation was purely experimental.

The backward facing step was also investigated by Durst and Rastogi [18] who performed flow measurements using a single channel Laser Doppler Anemometer and traversing apparatus. Comparisons were made with the k - $\epsilon$ model predictions using the code TEACH an upwind differencing finite difference computer code. There was considerable disagreement between the predicted velocity profiles and the measured profiles. Poor agreement was obtained in the separated flow regions as the code used the "law of the wall" which will not work at a point of

reattachment.

Smyth [19] examined the recirculation occurring with a symmetric sudden expansion. A LDA system was used for the flow measurements and no comparisons were made with turbulence models.

## 2.3 WALL JETS

In addition to an examination of the recirculating flow cavity, the incoming wall jet will also be examined in some detail.

The two dimensional wall jet is formed when a jet of fluid enters an "unbounded" area on one side with a wall surface on the other side. The jet will flow along the wall while fluid from the surrounding area is entrained into the jet [20]. This is the case for the recirculating flow cavity being investigated with the exception that the fluid within the flow cavity is not at rest due to the fact that the boundaries of the cavity confine the flow to some degree.

The turbulent wall jet has been analyzed analytically (Glauert [21]) by dividing the flow regime into two parts. The first region, the area between the wall boundary and the point of maximum velocity in the jet, is called the boundary layer region. Glauert theoretically found that the boundary layer region is governed by Blausius's formula and the second region containing the diffusing jet and the entraining fluid, called the outer layer, is governed by Prandtl's hypothesis. Matching of the inner and outer regions leads to a similarity type solution which applies to

both radial and plane wall jets. Kruka and Eskinazi [22] have done experimental work to confirm Glauert's initial analytical work. Swamy [23] has given experimental wall jet profiles for ratios of y the distance from the jet mouth over R incoming jet radius for the semi circular wall jet. The profiles presented gave good agreement with a similarity type solutions with the exception of the lower values of y/R. E. Foerthmann [24] found that the velocity profiles are similar if the region near the entrance is disregarded. The velocity profiles can be described by the equation:

$$v \propto y^{-1/2} f(x/y) \qquad (2.3.1)$$

This states that the velocity peak decreases as $y^{-1/2}$.

## 2.4 THEORY OF LASER DOPPLER ANEMOMETER OPERATION

Fundamentally, the Laser Doppler Anemometer (LDA) measures velocity by detecting the Doppler shift of light which is scattered from a moving particle.

The gas laser (He Ne in this study) is the foundation of the system as light which is spatially and temporally coherent is required.  Spatially coherent light is required as the light must be focussed to a reasonable measuring volume and must create interference patterns in space.  Temporally coherent light is required as pure light will have a nearly constant frequency.  The intensity of the beam at all cross sections has a Gaussian distribution, a property of all lasers, which will be used in the detection of the scattered light.

There are two common modes of operation of any LDA system and they are the reference beam mode and the differential or fringe mode.  In the reference beam mode, one beam is located at the measuring volume and the other unshifted "reference" beam from the same source is combined to make a detectable difference frequency.

The dual beam or fringe mode was used in this study as it gives the best signal to noise quality.  The dual

beam mode comprises of two equal intensity laser beams which cross at the measuring volume to be examined. When the beams cross they set up interference fringes of light and dark bands. A particle moving through this interference area will go through alternatively low light levels (dark band) and high light levels (light band). From geometric and optical properties (wavelength of the laser and focussing lens half angle) the spacing of the fringes will be known to be a constant $d_f$. The light which is scattered from this particle is detected by a photodetector which obtains the frequency of the scattered light. The particle velocity and hence the fluid velocity is obtained by multiplying the scattered frequency by the fringe spacing. As described, there is no way to determine the flow direction as the light frequency will be the same regardless of the direction the particle is moving in the flow. To overcome this difficulty frequency shifting is employed. As described above, the interference pattern set up by the two crossing beams is a stationary pattern in space. Frequency shifting shifts one of the beams such that the interference pattern will now no longer be stationary but due to the differing frequencies will be moving. In this way flow direction can be determined as a particle moving in the

direction of the fringes will have a lower frequency than a particle going at the same velocity in the opposite direction.

The system obviously depends on the presence of particles in the flow to shift the light frequency and tap water was found to contain enough seeding although artificial seeding was tested.

## 2.4.1 Frequency Shifting (Bragg Cell) Theory

Frequency shifting in this system is performed using Bragg interaction, a form of light-ultrasound interaction. A high frequency acoustic signal (40 MHz) is applied to a transducer bonded to a glass block within the Bragg cell mode. The wave travels in the glass and varies the index of refraction of the glass due to the peaks and troughs of the acoustic wave creating a moving diffraction grating. The laser beam will enter the glass block and several shifted laser beams will be generated and leave the cell including the initial unshifted beam. All beams are removed (higher order beams and the unshifted beam) except for the first order shifted beam.

# CHAPTER THREE

## DESCRIPTION OF THE EXPERIMENTAL APPARATUS

### 3.1 The Flow Cavity

The flow cavity was designed such that the geometry
could be assumed two dimensional (depth of cavity 5.0
cm). Flow visualization has confirmed this to be nearly
so. The reason this was done was to provide two
dimensional data as much as possible that could be
directly compared to two dimensional numerical simula-
tions. The assumption of two dimensionality simplified
the measurements considerably. The dimensions of the
cavity were 15.0 cm wide, 30.0 cm high and 5.0 cm deep.
Flow entered the cavity via a wall jet at the lower left
corner of the cavity in the horizontal plane. The
nozzle is 0.2 cm wide and 5.0 cm deep. A 20 cm flow
development length was incorporated into the cavity in
order to assure fully developed flow at the nozzle. The
flow exit was in the lower right corner of the cavity in
the same plane as the inlet. The outlet was in all
respects identical to the inlet being 0.2 cm wide and
5.0 cm deep in exit area and having the same exit length
(20 cm) as the 20 cm inlet development length. The

31

pressure in the cavity was monitored using a pressure gauge mounted at the top of the cavity (Figures 1 and 2) and the water temperature was monitored at the head tank.
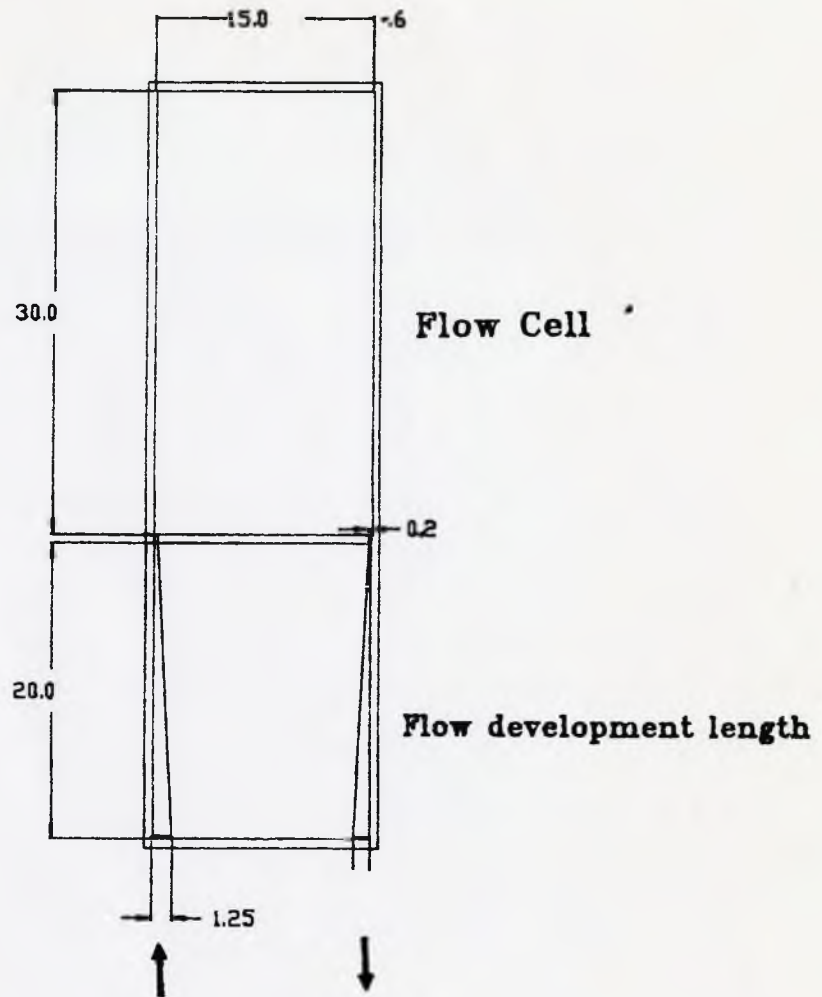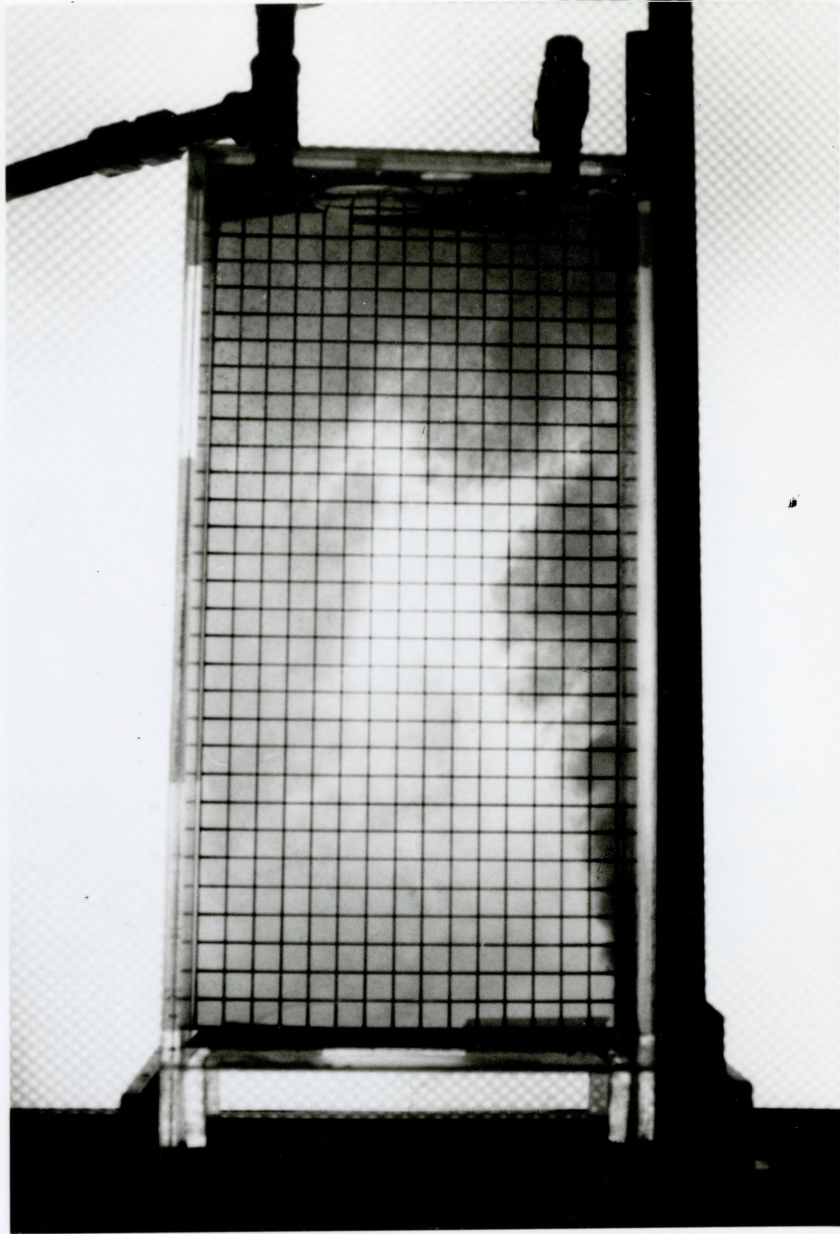
All dimensions in cm

Tank constructed of Plexiglas plastic

Tank is 5 cm deep

Figure 1 : Recirculating Flow Cell

Figure 2 : Recirculating Flow
Dye Injection
Grid 1 cm square

## 3.2 The Flow Loop

The cavity inlet and outlet were connected into the flow loop as shown in Figure 3. Water ran from the head tank to the centrifugal pump (Little Giant ) where the pump outlet was connected to a flow control valve and bypass which was connected to a variable area flowmeter (Brooks Rotameter A-8M-25-4). The water was then pumped to the inlet nozzle development length. The water would then circulate in the cavity before leaving the cavity via the exit opening and back to the head tank. Water flow rate was monitored on the flowmeter and the flow rate was controlled by the flow control valve downstream of the pump.
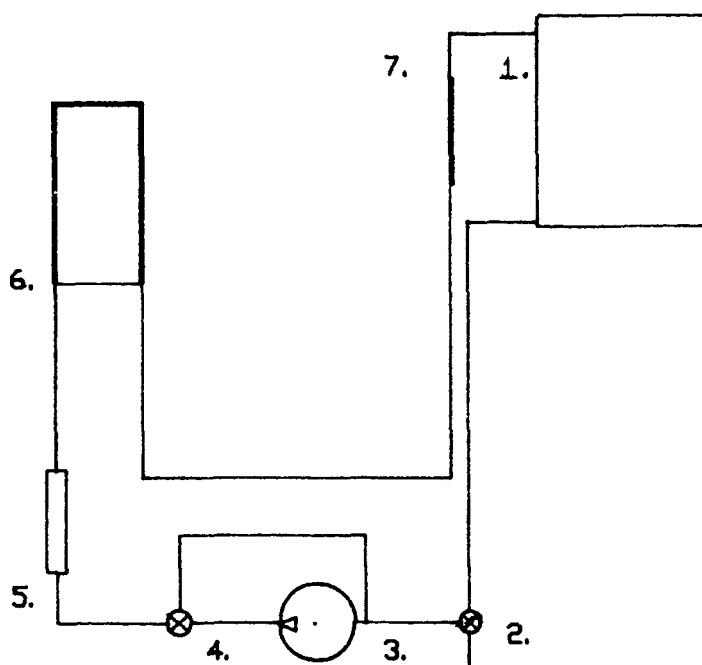
## COMPONENT LIST

1. HEAD TANK
2. DRAIN CONTROL
3. PUMP
4. FLOW CONTROL VALVE
5. FLOWMETER
6. RECIRCULATING FLOW CAVITY
7. RETURN LINE

**Figure 3 : Flow Loop Schematic Diagram**
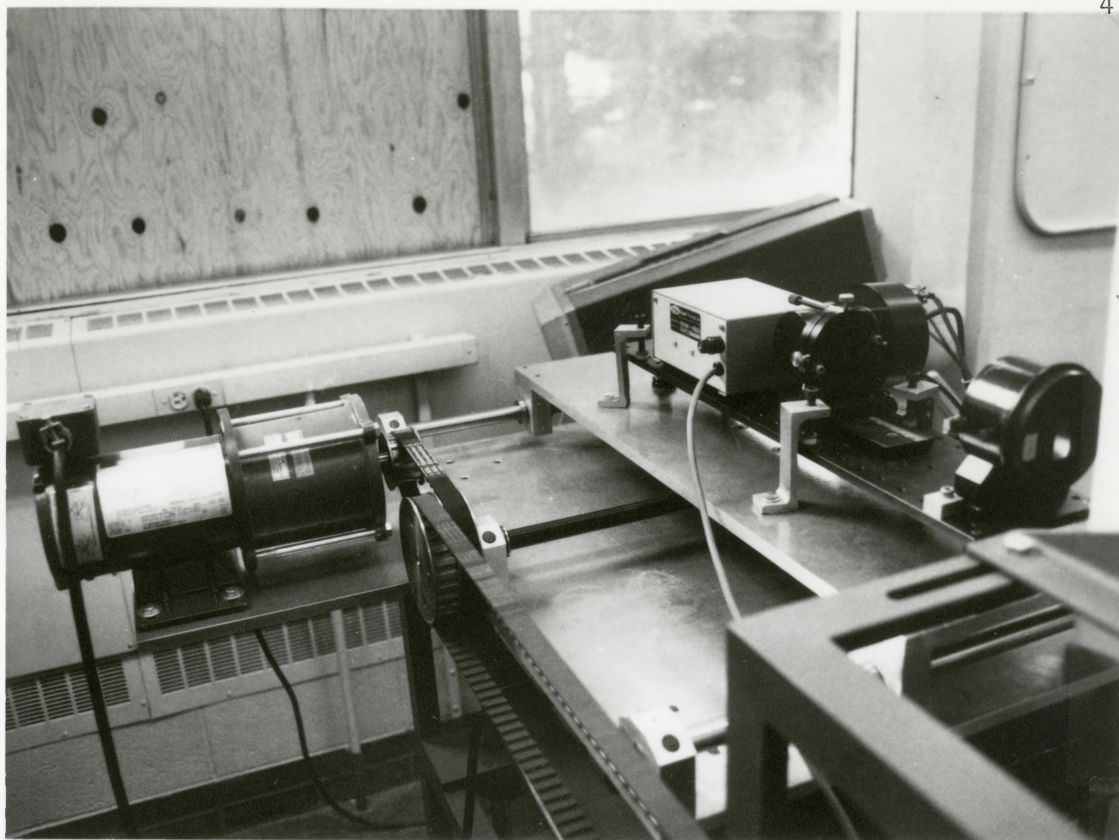
## 3.3 Traversing Mechanism

In the present case study the model was held fixed
in the test supports.  The sending and receiving optics
were moved and positioned at the required coordinates of
the model by means of specially designed traversing
tables.  Both tables were moved synchronously by toothed
belts and leadscrews.  Speed and position could be
controlled with the variable speed DC motor controller.
One DC motor drove both tables in the vertical direction
and the second motor mounted on the receiving optics
table controlled motion in the horizontal plane (Figures
4,5 and 6).
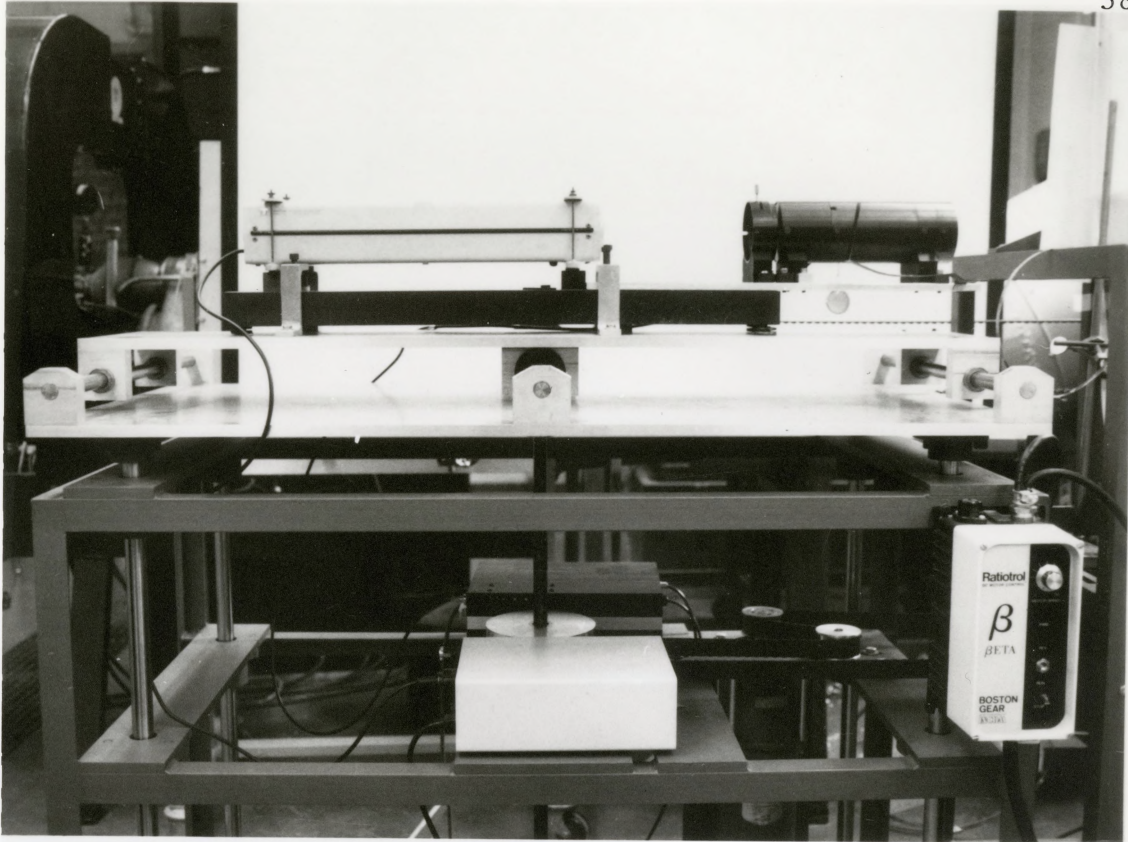
Figure 4 : Traversing Mechanism
Sending Optics
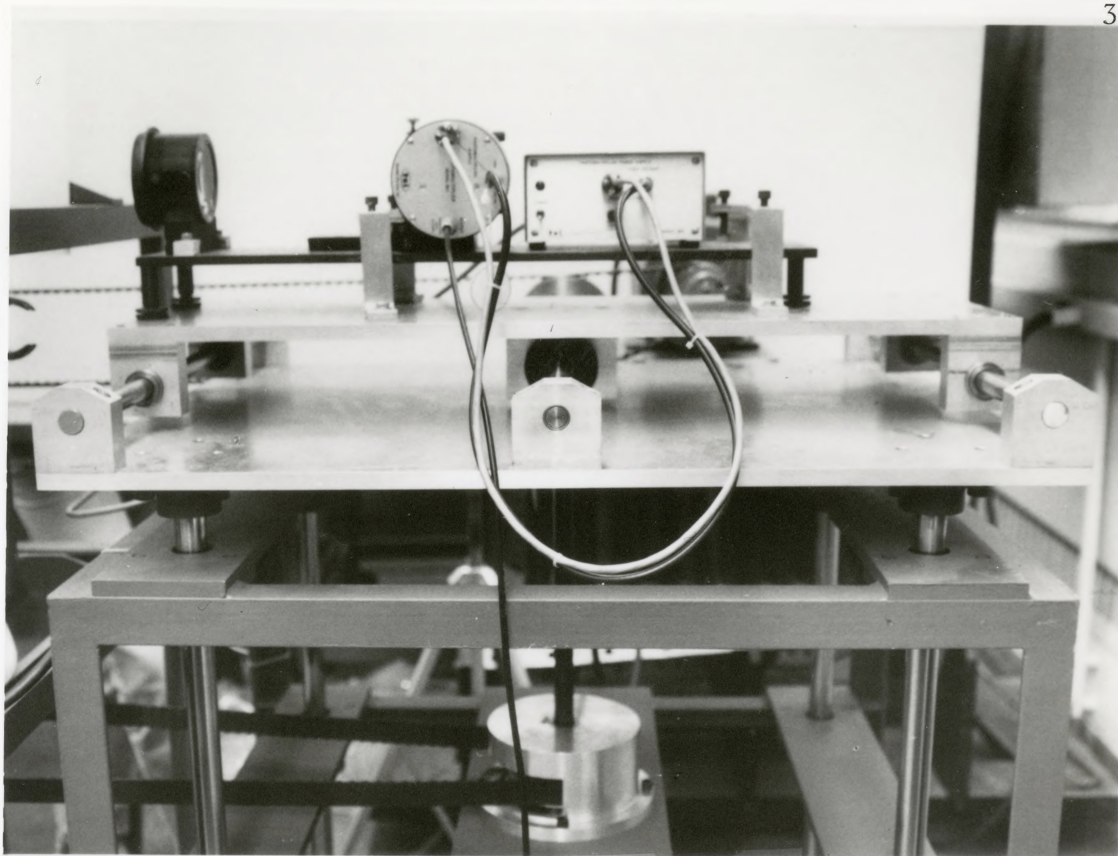
Figure 5 : Traversing Mechanism
Receiving Optics

Figure 6 : Traversing Mechanism
Horizontal Traverse

## 3.4 Laser Doppler Anemometer Apparatus

The single component LDA system was set up to operate in the dual beam forward scatter mode with the receiving optics in line with the transmitting optics. This was chosen as it provided optimum signal quality. The LDA system will now be described in some detail (Figure 7). A 5 mW Helium Neon Laser (Spectra Physics Model 120) (Figure 8 - a) was mounted at the back of the transmitting optics table. In line with the beam were the transmitting optics (Figure 8). The transmitting optics consisted of a beam polarizer (Figure 8 - b) which was rotated depending on the measurement axis. The next component was the beamsplitter (Figure 8 - c) which split the single laser beam into two components of equal intensity 50 mm apart or 25 mm from the original beam. The beamsplitter could be rotated to obtain differing velocity components of interest. Adjacent to the beamsplitter was the Bragg cell (Figure 8 - d) which was used to frequency shift one of the beams in order to detect flow reversals. This component could also be rotated for other velocity components. The beams were then focussed using a lens (Fd = 243 mm) (Figure 8 - e). The measuring volume was at the intersection of the two beams.

On the receiving optics table, the first component was the receiving lens (Fd = 250 mm) (Figure 9 - a) which was covered partially to eliminate the strong unscattered beams from the laser and to allow only the shifted doppler light through. The scattered light was then focussed using a lens (Fd = 200 mm) (Figure 9 - b) onto the photomultiplier tube (Figure 9 - c). The signal which was converted from light to voltage by the photomultiplier went to the Bragg cell module before going to the Dantec 55L90a LDA Counter Processor (Figure 10).
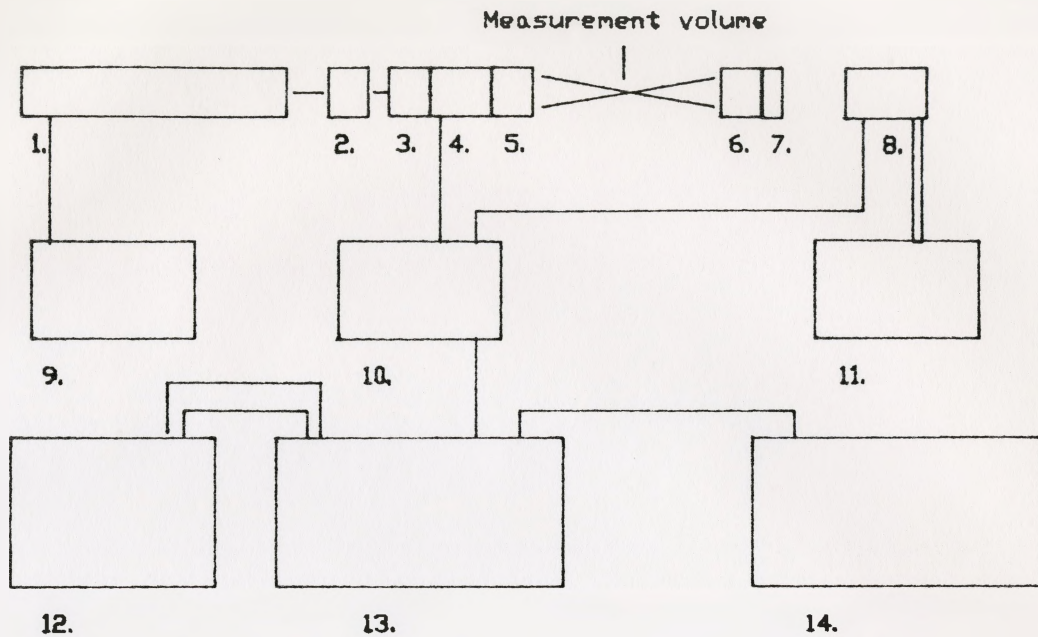
**COMPONENT LIST**

1. Spectra Physics Model 120 HeNe Laser (5 mW)
2. TSI Model 902 Polarization Rotator
3. TSI Model 915 Beamsplitter
4. TSI Model 982 Bragg Cell Optical Module
5. TSI Model 918 Focussing Lens (Fd = 243 mm)
6. TSI Model 938 Receiving Lens (Fd = 240 mm)
7. TSI Model 935 Receiving Lens (Fd = 200 mm)
8. TSI Model 962 Photomultiplier
9. Spectra Physics Laser Exciter
10. Tsi Model 985 Bragg Cell Frequency shifter
11. TSI Model 965 Photomultiplier Power Supply
12. Tektronix Model 7613 Oscilloscope
13. Dantec Model 55L90a LDA Counter Processor
14. Tatung TCS-7000 AT computer

**Figure 7 : LDA Component Block Diagram**
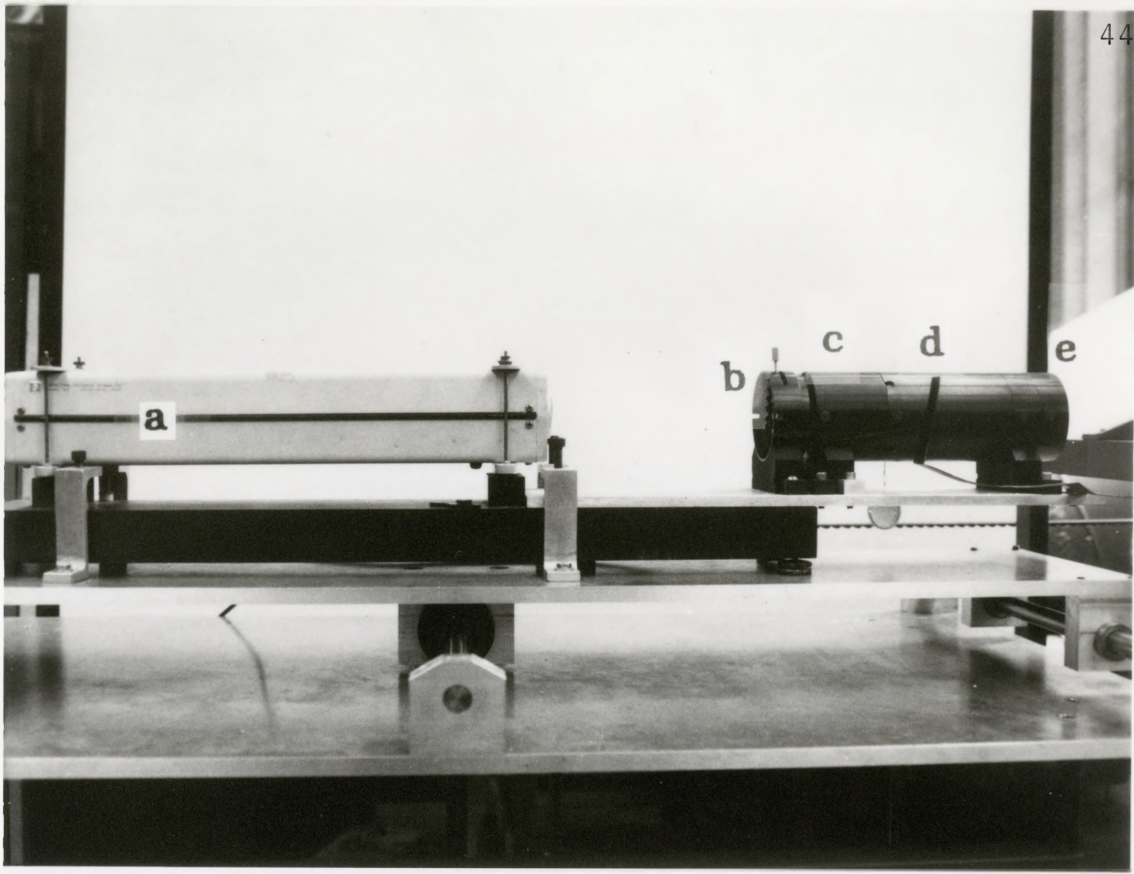
a − He Ne Laser
b − beam polarizer
c − beamsplitter
d − Bragg Cell
e − focussing lens

Figure 8 : LDA Sending Optics
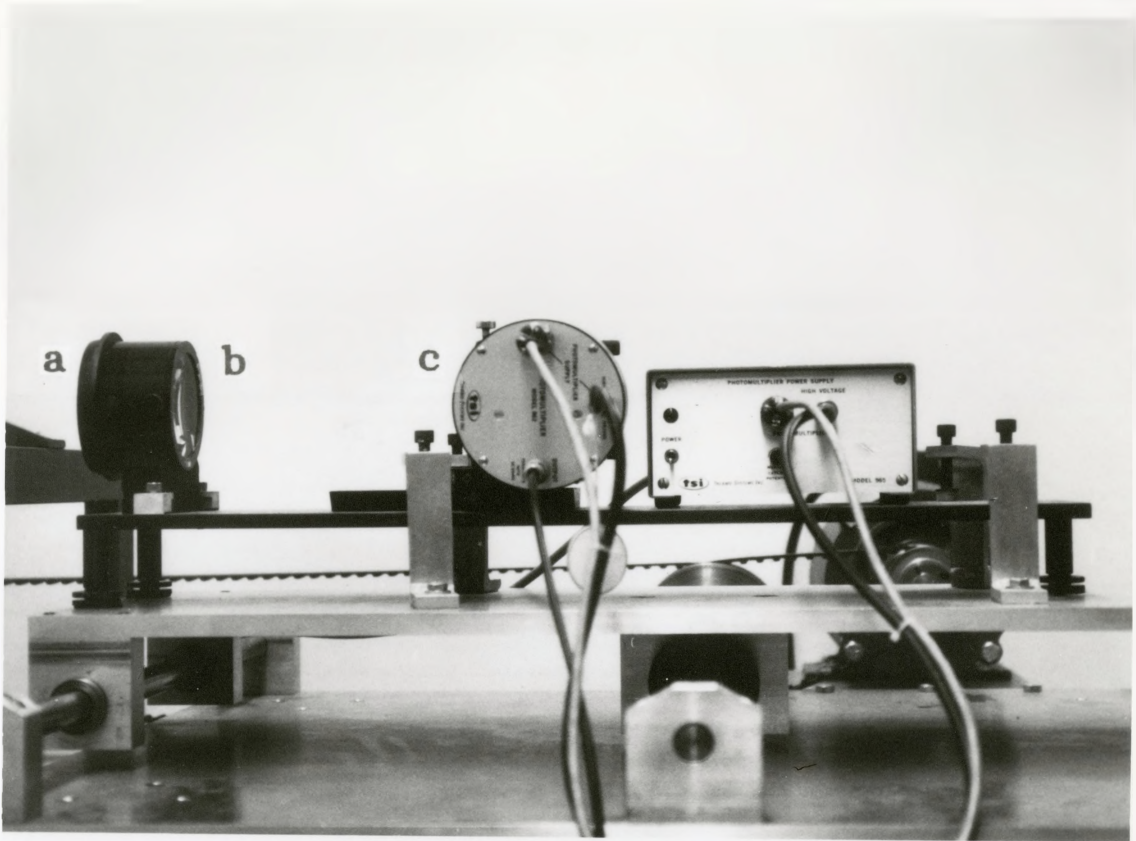
a — receiving lens
b — focussing lens
c — photomultiplier

Figure 9 : LDA Receiving Optics and
Photomultiplier

## 3.5 Counter Processor

The Counter Processor determines the time a scattering particle takes to pass through a known number of interference fringes within the measurement volume. This time and distance then give the instantaneous velocity of that particle.

The fixed number of fringes mode on the counter processor times the particle over 5 periods or fringe counts (Low count) and over 8 periods (High count) at a 500 MHz clock speed. This mode was used exclusively as it gives the best results when there is more than one particle in the measuring volume and when there are poor signal to noise ratios.

To avoid erroneous data collection a comparator is built in to the counter. This unit checks to see if a percentage (selectable) of the high count (8 periods) is always greater than the difference between the high count and the low count (5 periods). The comparator was set at 3 % accuracy for all measurements.

The amplifier gain was used to attenuate the preamplifier output when the signal level was too high. The threshold window was used to set the amplitude threshold of incoming signals and therefore removed signals from large scattering particles. Filters were

used to remove background noise picked up by the photomultiplier (low and high pass) and also to remove the Doppler pedestal signal (high pass).

Digital data from the Counter Processor was transmitted to the Tatung TCS 700 AT computer via the Dantec 92G35 DMA interface board. The data output contained two binary outputs the Fringe Number (8 bit binary) and the Passage Time for 8 fringes (14 bit binary) (Figure 10).
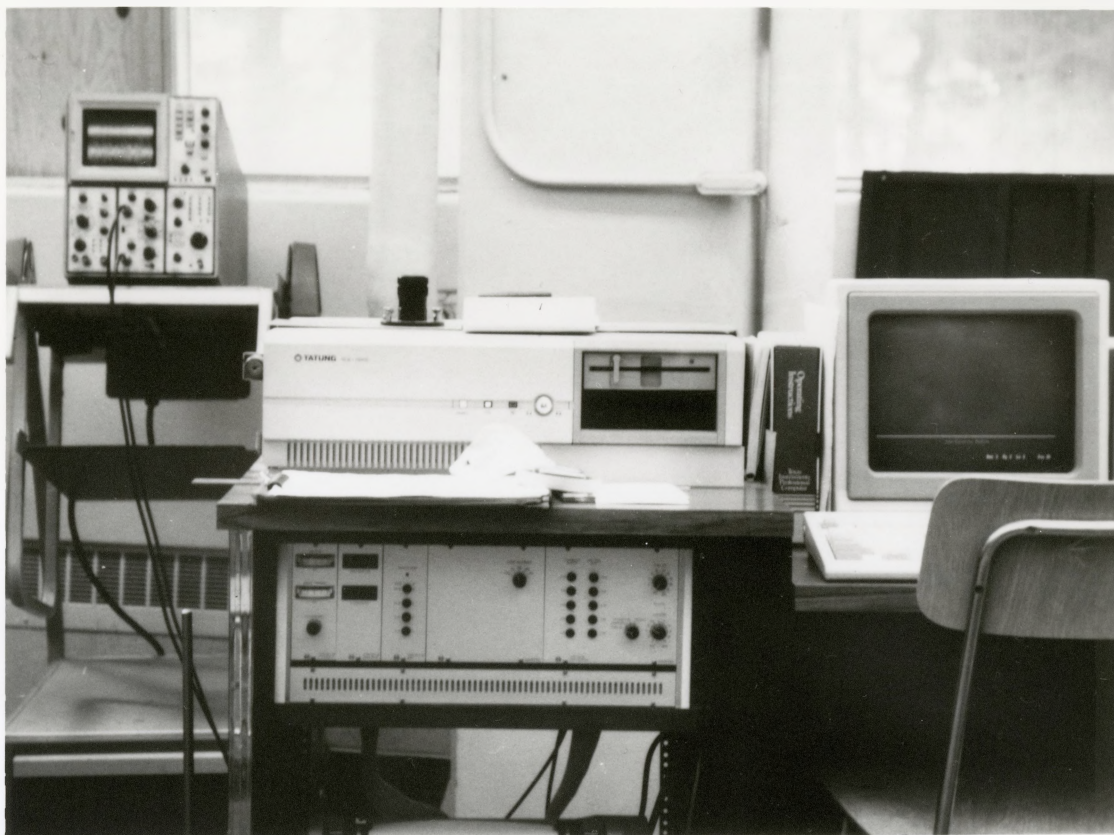
Figure 10 : LDA Counter Processor
Data Acquistion Computer
Oscilloscope

# CHAPTER FOUR

## EXPERIMENTAL PROCEDURE

Initially, the flow loop was commissioned with all components being examined for leaks. The flowmeter (Brooks Rotameter) was then calibrated over the range of use.

## 4.1 Flow Visualization

In order to fully understand the flow patterns present flow visualization studies were performed. Flow visualization can be classified into three main categories based on the physical principles which are involved in the technique [25]. The three main categories are the addition of a visible foreign material, visualization by means of fluid density variations, and energy input to rarefied gas flows.

The only technique which applies in this study is the addition of visible foreign material. The motion of the foreign material in the fluid is observed instead of the fluid itself.

The flow visualization techniques employed were the use of water soluble dye, laser slit lighting with tracer

particles, and laser slit lighting due to a rotating mirror.

The water soluble dye (potassium permanganate, a dark purple dye) was injected into the flexible tubing just before the entry development length. This method provided visual representation of overall flow patterns. These were recorded using both a video camera and a 35 mm still camera.

The second method used the laser focussed on a cylindrical lens to provide a thin slit of light which cut a plane of light within the cavity. Polystyrene particles were used as tracers to reflect the laser light. This method provided a detailed analysis of a specific area of the cavity. The use of the rotating mirror gave similar results to the laser and cylindrical lens method detailed above. In this method the laser beam is directed onto a mirror which rotates with a known frequency. High frequency rotation of the mirror creates a slit which illuminates a plane in the cavity similar to the laser and cylindrical lens method [26]. Using these visual aids areas of interest were discovered for further investigation with measurements.

## 4.2 Cavity Flow

Two cases of the entire cavity were examined. For the first case a low flow rate was chosen (Re jet = 1167) and a very detailed grid was chosen. The grid spacing was chosen such that there would be readings every 5 mm vertically and horizontally for the first 65 mm and 5 mm spacing horizontally and 10 mm spacing vertically for the remaining 235 mm (Table 2)(Figure 11). Such a fine grid (29 X 36) was chosen to give detailed analysis of the flow pattern present.

| Grid number | Spacing (mm) | | Grid number | Spacing (mm) | |
|---|---|---|---|---|---|
| 1 | 5 ✗ | 5 △ | 24 | 120 ✗ | 175 △ |
| 2 | 10 | 10 | 25 | 125 | 185 |
| 3 | 15 | 15 | 26 | 130 | 195 |
| 4 | 20 | 20 | 27 | 135 | 205 |
| 5 | 25 | 25 | 28 | 140 | 215 |
| 6 | 30 | 30 | 29 | 145 | 225 |
| 7 | 35 | 35 | 30 | | 235 |
| 8 | 40 | 40 | 31 | | 245 |
| 9 | 45 | 45 | 32 | | 255 |
| 10 | 50 | 50 | 33 | | 265 |
| 11 | 55 | 55 | 34 | | 275 |
| 12 | 60 | 60 | 35 | | 285 |
| 13 | 65 | 65 | 36 | | 295 |
| 14 | 70 | 75 | | | |
| 15 | 75 | 85 | | | |
| 16 | 80 | 95 | | | |
| 17 | 85 | 105 | | | |
| 18 | 90 | 115 | | | |
| 19 | 95 | 125 | | | |
| 20 | 100 | 135 | | | |
| 21 | 105 | 145 | | | |
| 22 | 110 | 155 | | | |
| 23 | 115 | 165 | | | |

✗    x direction (measured from tank wall)

△    y direction (measured from tank wall)

## Table 2
## Grid Spacing for Re = 1176

y
x

— 1 cm
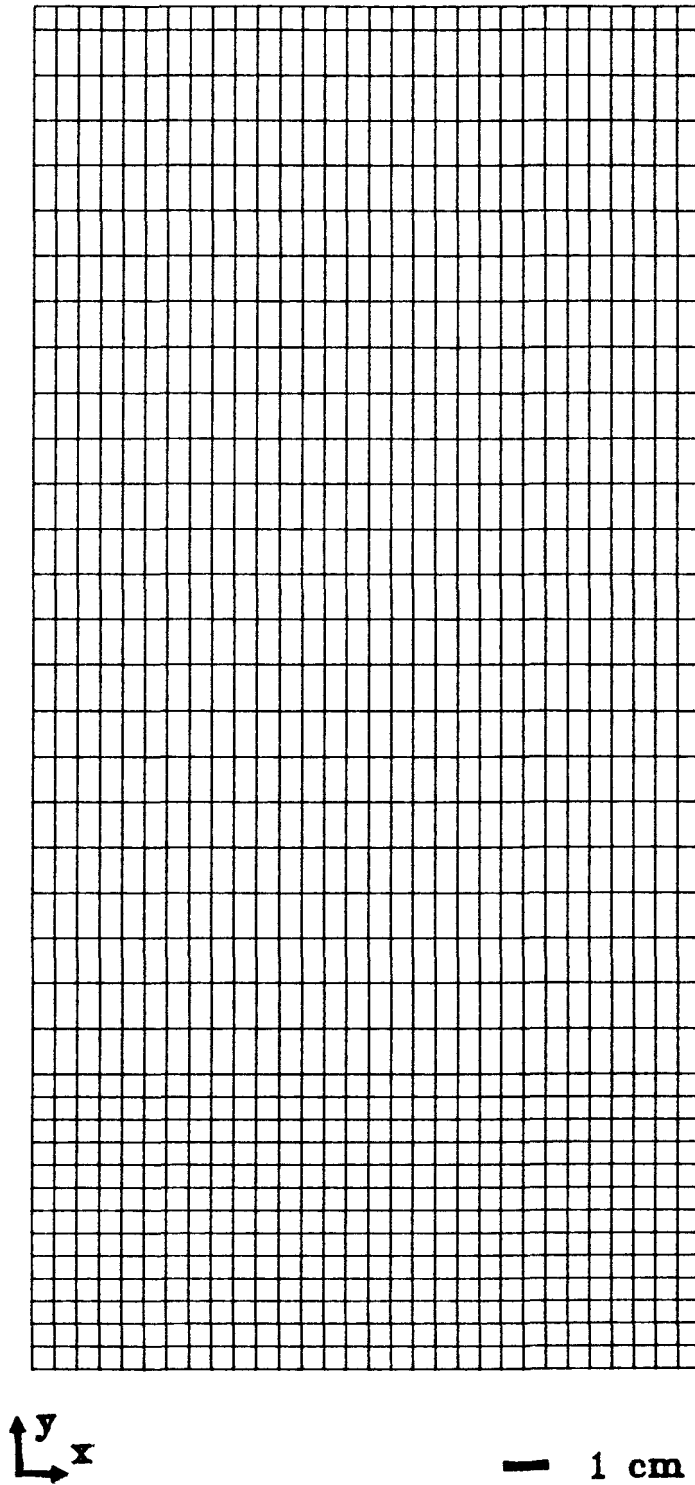
Figure 11 : Grid Spacing (29 X 36)
Re nozzle = 1176

For the second case of the entire cavity a higher flow rate was chosen (Re jet = 3231) and a variable spacing grid was selected. This was done as the majority of flow of interest occurred around the periphery of the cavity with the centre section of the cavity remaining almost stagnant. Thus cells were chosen as shown in Table 3 (Figure 12). Both cases chosen gave good analysis of the flow present.

| Grid number | Spacing (mm) | Spacing (mm) |
|---|---|---|
| 1 | 1.25 | 2.5 |
| 2 | 2.5 | 5. |
| 3 | 5 | 10. |
| 4 | 10 | 20. |
| 5 | 15 | 40. |
| 6 | 25 | 60. |
| 7 | 35 | 80. |
| 8 | 55 | 100. |
| 9 | 75 | 120. |
| 10 | 95 | 140. |
| 11 | 115 | 160. |
| 12 | 125 | 180. |
| 13 | 135 | 200. |
| 14 | 140 | 220. |
| 15 | 145 | 240. |
| 16 | 147.5 | 260. |
| 17 | 148.75 | 280. |
| 18 | | 290. |
| 19 | | 295. |
| | x direction | y direction |
| | (measured from tank wall) | (measured from tank wall) |

## Table 3
## Grid Spacing for Re = 3231
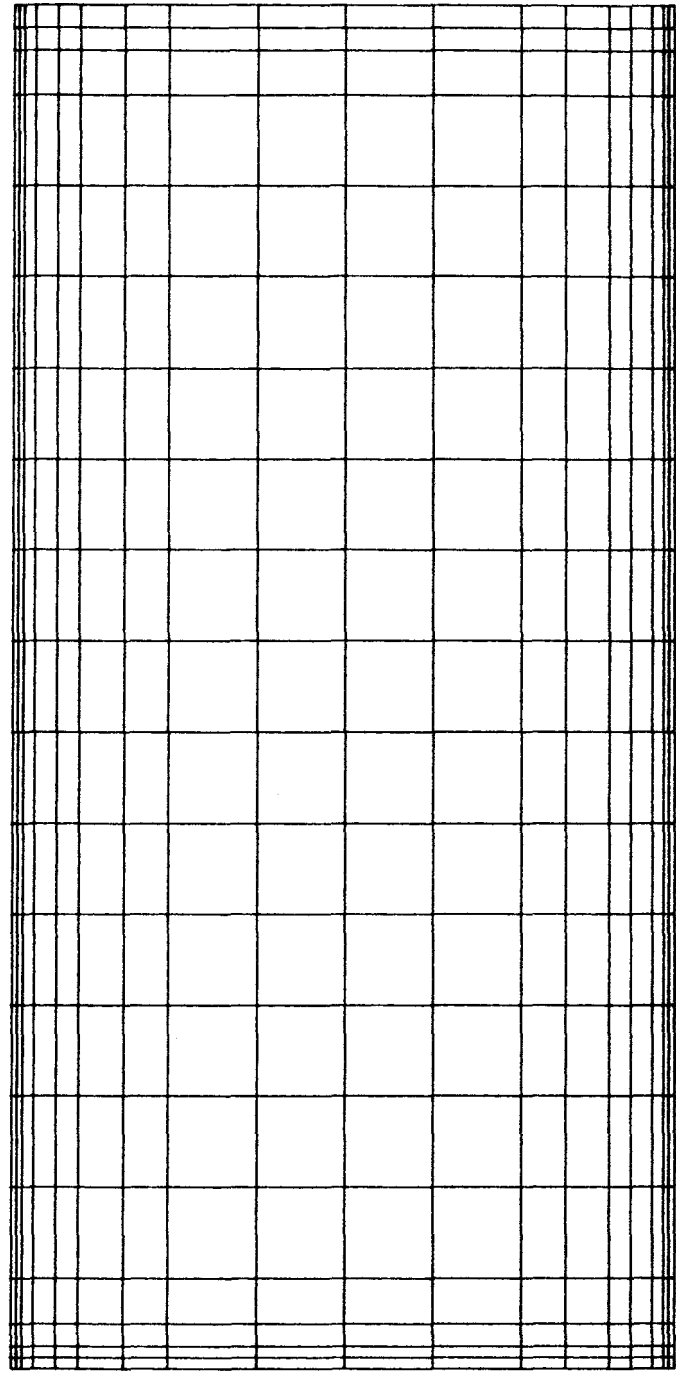
Figure 12 : Grid Spacing (17 X 19)
Re nozzle = 3231

### 4.3 Wall Jet

As another point of interest measurements were taken in the diffusing jet area in order to get a profile of the developing jet and compare these results with published data.  The measurements were taken every millimetre for 12 mm horizontally beginning at a cavity height of 8 mm ($y/L = 4$) and proceeding vertically every 4 mm to 36 mm ($y/L = 18$).  All measurements taken were obtained at the cavity centreline ($z = 2.5$ cm) with 2000 points taken for each mean velocity calculation.

### 4.4 LDA Counter Set Up

For the lower flow rate case (Re jet = 1167 ) the mode selector was set on Fixed number of fringes (8) with the amplifier gain set to -7 db and the threshold window set to 31 db and the comparator set to 3 %.  The Bragg cell was set at 100 kHz with the high pass filter set at 16 kHz and the low pass filter set at 256 kHz. This was done as the expected highest (area averaged) velocity at the jet entrance was 26 cm/s (equiv 82.54 kHz)

In the higher flow rate case (Re jet = 3231 ) the mode selector was again Fixed Nf with the amplifier gain

set to -7 db, the threshold window set to 31 db and the comparator set to 3 %.   The Bragg cell shift frequency was set at 500 kHz and the high pass filter set at 64 kHz and the low pass filter set at  1 MHz.   This was done as an area averaged flow rate of 72 cm/s (227 kHz) was expected at the jet entrance.

For all measurements taken the incoming data rate ranged from 6 to 10 kHz with a validation rate between 65 and 95 %.

# CHAPTER FIVE

# DESCRIPTION OF THE COMPUTER CODE

## 5.1 The Governing Equations

The governing equations are the conservation equations for transient two dimensional turbulent flow using the k - $\epsilon$ turbulence model. The equations are listed below.

Continuity

$$\frac{\partial u}{\partial x} + \frac{\partial v}{\partial y} = 0 \qquad (5.1.1)$$

x Momentum

$$\frac{\partial u}{\partial t} + \frac{u \partial u}{\partial x} + \frac{v \partial u}{\partial y} = -\frac{1}{\rho}\frac{\partial P}{\partial x} + \frac{1}{\rho}\frac{\partial}{\partial x}\left[\mu_e\frac{\partial u}{\partial x}\right] + \frac{1}{\rho}\frac{\partial}{\partial y}\left[\mu_e\frac{\partial u}{\partial y}\right]$$

$$+ \frac{1}{\rho}\frac{\partial}{\partial x}\left[\mu_e\frac{\partial u}{\partial x}\right] + \frac{1}{\rho}\frac{\partial}{\partial y}\left[\mu_e\frac{\partial v}{\partial x}\right] - \frac{2}{3}\frac{\partial k}{\partial x} \qquad (5.1.2)$$

59

**Y Momentum**

$$\frac{\partial v}{\partial t} + \frac{u\partial v}{\partial x} + \frac{v\partial v}{\partial y} = -\frac{1}{\rho}\frac{\partial P}{\partial y} + \frac{1}{\rho}\frac{\partial}{\partial x}\left[\mu_e\frac{\partial v}{\partial x}\right] + \frac{1}{\rho}\frac{\partial}{\partial y}\left[\mu_e\frac{\partial v}{\partial y}\right]$$

$$+ \frac{1}{\rho}\frac{\partial}{\partial x}\left[\mu_e\frac{\partial u}{\partial y}\right] + \frac{1}{\rho}\frac{\partial}{\partial y}\left[\mu_e\frac{\partial v}{\partial y}\right] - \frac{2}{3}\frac{\partial k}{\partial y} \quad (5.1.3)$$

**Turbulent Kinetic Energy**

$$\frac{\partial k}{\partial t} + \frac{u\partial k}{\partial x} + \frac{v\partial k}{\partial y} = \frac{1}{\rho}\frac{\partial}{\partial x}\left[\frac{\mu_e}{\sigma_k}\frac{\partial k}{\partial x}\right] + \frac{1}{\rho}\frac{\partial}{\partial y}\left[\frac{\mu_e}{\sigma_k}\frac{\partial k}{\partial y}\right] + G - \epsilon$$

$$(5.1.4)$$

**Rate of Dissipation of Kinetic Energy**

$$\frac{\partial \epsilon}{\partial t} + \frac{u\partial \epsilon}{\partial x} + \frac{v\partial \epsilon}{\partial y} = \frac{1}{\rho}\frac{\partial}{\partial x}\left[\frac{\mu_e}{\sigma_e}\frac{\partial \epsilon}{\partial x}\right] + \frac{1}{\rho}\frac{\partial}{\partial y}\left[\frac{\mu_e}{\sigma_e}\frac{\partial \epsilon}{\partial y}\right]$$

$$+ C_1\frac{\epsilon}{k}G - C_2\frac{\epsilon^2}{k} - C_3\frac{\epsilon}{k} \quad (5.1.5)$$

and G is defined as

$$G = \frac{\mu_t}{\rho} \left[ \ 2 \ \left[\frac{\partial u}{\partial x}\right]^2 + \ 2 \ \left[\frac{\partial v}{\partial y}\right]^2 \ + \left[ \ \frac{\partial u}{\partial y} + \frac{\partial v}{\partial x} \right]^2 \ \right] \qquad (5.1.6)$$

## 5.2 The Solution Scheme

The computer code FONS-TURB [28] uses the finite difference approach for solution of the Navier Stokes equations. The code solves the two dimensional transient Navier Stokes equations by means of two dimensional control volume cells of variable dimensions $\Delta x_i$ and $\Delta y_j$ . Velocities are located at the control volume boundaries while all other dependant variables are located at the cell centre (staggered grid). This procedure was adopted to eliminate difficulties in having the pressure and velocity terms at the same location [27]. Using this scheme the pressure difference between adjacent grid points becomes the driving force for the velocity component between these grid points. Convective terms in the conservation equations were upwind finite differenced and diffusion terms were finite differenced in the fully conservative form as effective diffusivities were functions of

dependant variables. The explicit form of the equations was used to advance the time step [28].

The difference equations will remain stable as long as the fluid is not permitted to cross more than one cell in one time step. Thus the time step must be

$$\Delta t < \min \left\{ \frac{\Delta x_{ij}}{|\overline{U}_{ij}|} , \frac{\Delta y_{ij}}{|\overline{V}_{ij}|} \right\} \qquad (5.2.1)$$

where the minimum is the smallest of all cells in the mesh.

## 5.3 Wall Functions

Near the solid walls the flow field is directly affected by the wall boundary. In this affected region, the "inner" region, there are large gradients of most flow parameters and as a result boundary conditions are difficult to impose. Closely spaced grid nodes are required to model the gradients. Alternatively, to overcome excessive computing costs the FONS-TURB code uses the wall function method which employs empirical laws to predict the near wall flow field. Near the wall

the turbulent velocity flow field consists of two basic regions the laminar sublayer and the logarithmic region. These regions are defined by the dimensionless distance from the wall $y^+$.

$$y^+ = \frac{u_\tau \, y_p \, \rho}{\mu} \qquad (5.3.1)$$

where $y_p$ is the normal distance to the cell centre

$$u_\tau = \sqrt{\frac{\tau_w}{\rho}} \qquad \text{is the friction velocity}$$

The division between the two regions is defined as

$0 < y \leq 11.63$      laminar sublayer

$11.63 < y \leq 100$      logarithmic region

The near wall nodes are chosen to be located in the logarithmic region for which the turbulent kinetic energy equation and the dissipation rate equation are modified as follows.

Turbulent kinetic energy

$$\frac{\partial k}{\partial t} + \frac{u \partial k}{\partial x} + \frac{v \partial k}{\partial y} = \frac{1}{\rho} \frac{\partial}{\partial x} \left[ \frac{\mu_e}{\sigma_k} \frac{\partial k}{\partial x} \right]$$

$$+ \frac{1}{\rho} \frac{\partial}{\partial y} \left[ \frac{\mu_e}{\sigma_k} \frac{\partial k}{\partial y} \right] + G - \epsilon \qquad (5.3.2)$$

where G is modified near a bottom horizontal wall

$$\overline{G} = G - \frac{\mu}{\rho} t \left[ \frac{\partial u}{\partial y} \right]^2 + \frac{\tau_w}{\rho} \frac{u_p}{y_p} \qquad (5.3.3)$$

The wall shear stress $\tau_w$ is given by

$$\tau_w = \frac{u_p \rho C_\mu^{1/4} k_p^{1/2} \kappa}{\ln \left[ \dfrac{9 y_p \rho C_\mu^{1/4} k_p^{1/2}}{\mu} \right]} \qquad (5.3.4)$$

where $u_p$ is the tangential velocity

The dissipation term is modified as

$$\bar{\epsilon} = \frac{C_\mu^{3/4} k_p^{3/2}}{\kappa \, y_p} \, \ln\left[ \frac{9 \, y_p \rho \, C_\mu^{1/4} k_p^{1/2}}{\mu} \right] \qquad (5.3.5)$$

## 5.4 Code Algorithm

The basic steps which the code follows are outlined in Figure 13. Initially, the grid size and node locations are input as well as constants such as turbulence model constants and time step and fluid property values. The program then enters the iterative cycle. Velocities are then calculated explicitly from the momentum equations using previous time values. The velocity boundary conditions are then input. The new velocities normally will not satisfy the continuity equation which is a constraint to be satisfied.

$$0 = \frac{(U_{ij} - U_{i-1j})}{\Delta x_{ij}} + \frac{(V_{ij} - V_{i-1j})}{\Delta y_{ij}} \qquad (5.4.1)$$

The pressures are then tested for convergence and if not converged the cell pressures are adjusted. The velocities are then updated until convergence occurs. Once converged, the kinetic energy and dissipation energy are calculated. The time is then advanced for the next loop until the pre-specified time has been reached.
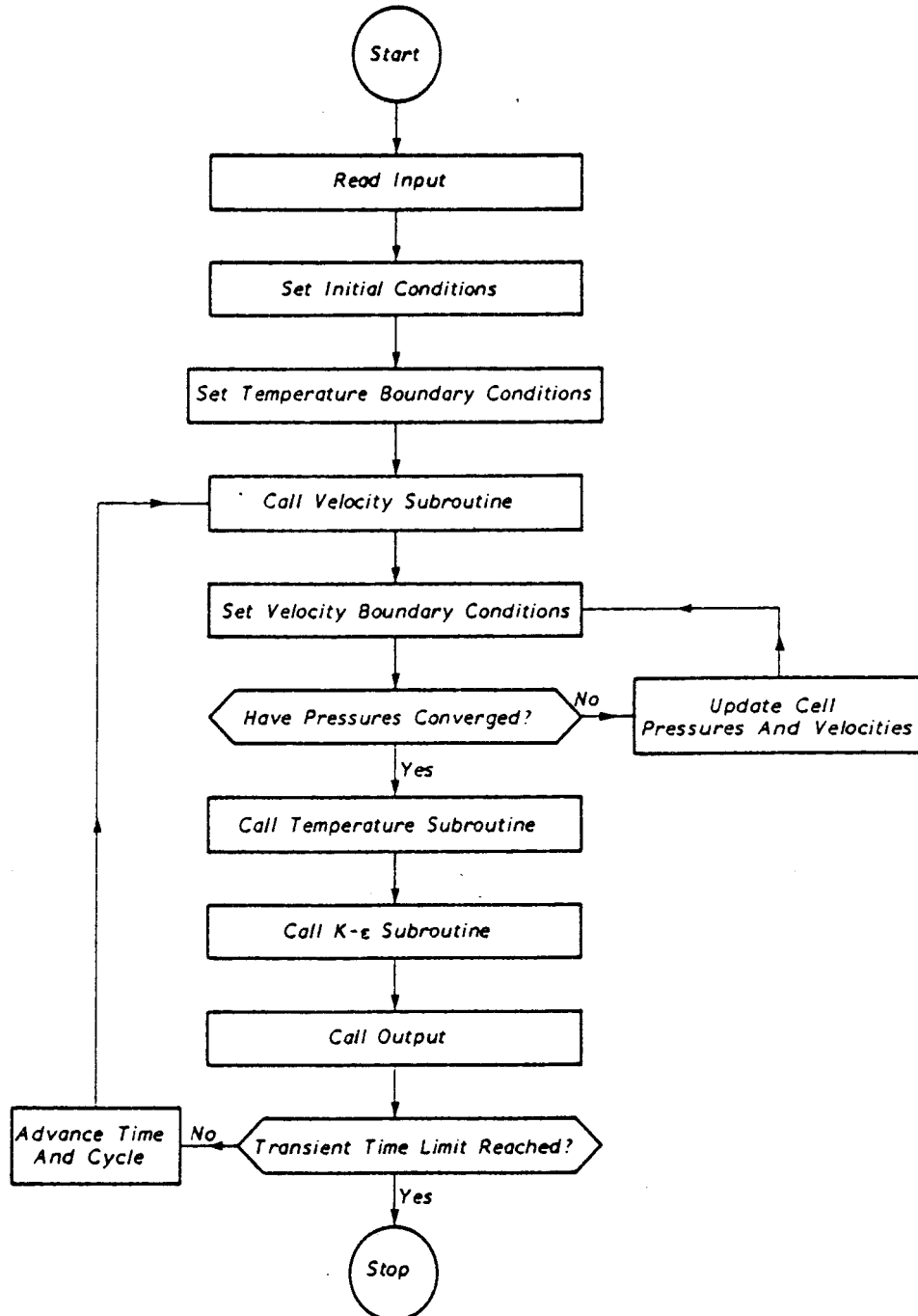
**Figure 13 : FONS TURB code algorithm**

## 5.5 Constants Used

For the k - $\epsilon$ model Launder and Spalding [29] recommend the use of the following constants (Table 4).

As the flow being investigated was isothermal fluid properties remained constant and are listed in Table 4.

| Constant | Value |
|----------|-------|
| C1 | 1.44 |
| C2 | 1.92 |
| $\sigma_k$ | 1.0 |
| $\sigma_e$ | 1.22 |
| Cμ | 0.09 |

Properties at 20° C

| | |
|---|---|
| Density | 997 kg/m$^3$ |
| Viscosity | .857 E-3 $\frac{kg}{ms}$ |

Table 4

Empirical Constants for k ε model

Fluid Properties

## 5.6 Boundary Conditions

The boundary conditions which were input to the program were the no slip boundary condition at the wall i.e. u = 0 at horizontal walls and v = 0 at vertical walls and the solid wall boundary condition u = 0 at vertical surfaces and v = 0 at horizontal surfaces. The exception to these conditions would be the prescribed inlet and outlet conditions. The grid was defined such that the jet width (2 mm) was broken into three equal area cells in the cavity. Thus the inlet conditions for the cell were prescribed based on a parabolic flow profile. To preserve continuity the outlet was prescribed in the same manner. The inlet kinetic energy and dissipation rate were prescribed at the inlet also. Inlet kinetic energy was based on a value found during the experimental analysis of the flow cavity. Inlet kinetic energy was varied for several runs of the code to see the effect of this parameter.

## 5.7 Grid Configuration

The grid was configured such that there would be more cells close to the walls and there were 23 grids in both the x and y directions (Figure 14). As the jet

entered the cavity at the wall the grid was divided into three cells the width of the jet as noted above.
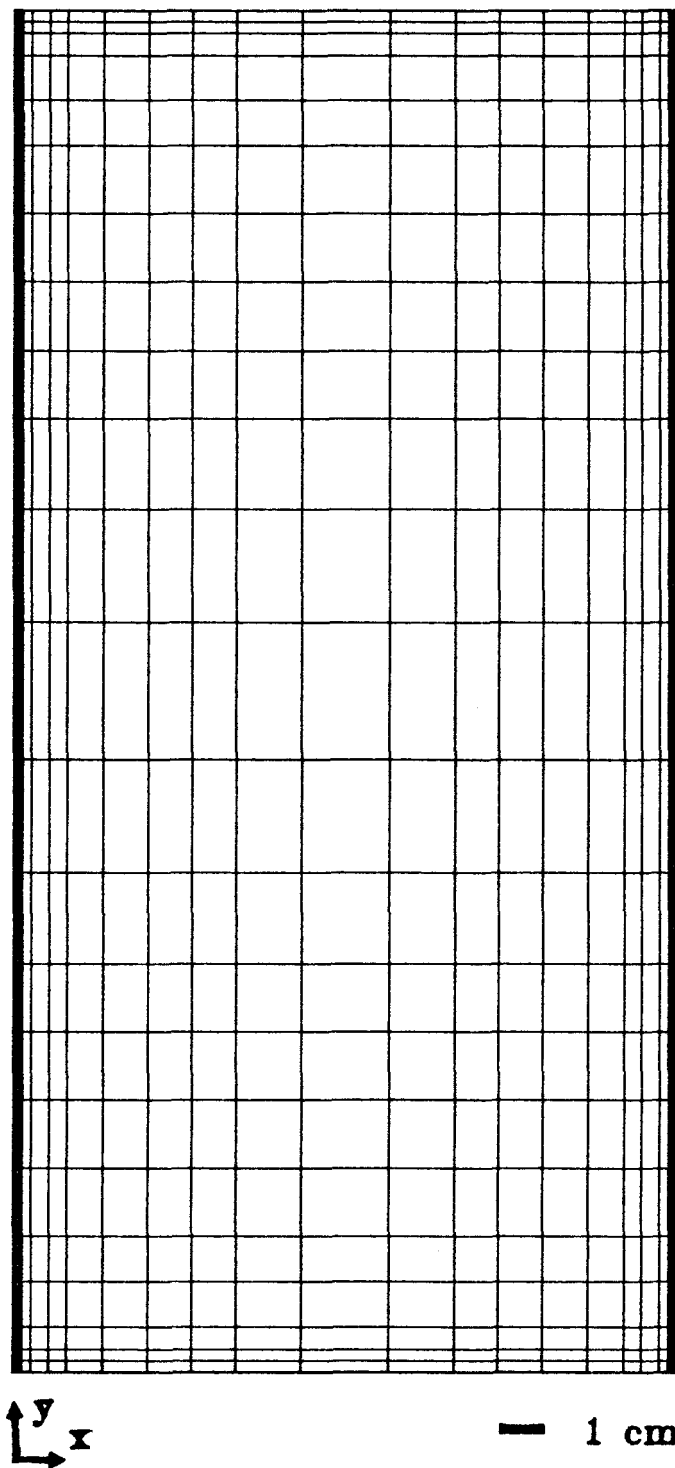
Figure 14 : Computational Grid (23 X 23)

# CHAPTER SIX

## RESULTS

## 6.1 EXPERIMENTAL RESULTS

### 6.1.1 Incoming Jet

In order to validate the measured velocity profiles, the measured inlet wall jet profiles were compared with existing known experimental and analytical work.

In order to compare these measurements with previously published similarity solution data the results were non dimensionalized. Vertical velocity V is divided by the maximum velocity present at that cavity height (Vm) and horizontal distance x is divided by distance x  where the velocity is one half of the maximum.  These values are then plotted for the differing cavity heights.  These values are then compared with the work of Swamy [30] (Figure 15).  As can be seen from the plot comparing the measurements of Swamy all the measured data fall with scatter along the published data line.  The reason for poor agreement in the lower values of y/L is probably due to the fact that

this solution depends on the location and evaluation of the maximum velocity present. At the lower values of y/L it was optically impossible to obtain measurements very close to the wall where the peak velocities of the wall jet would appear. Other measured values fall along the line predicted by the similarity solution and accordingly increases the reliability of the measurements.
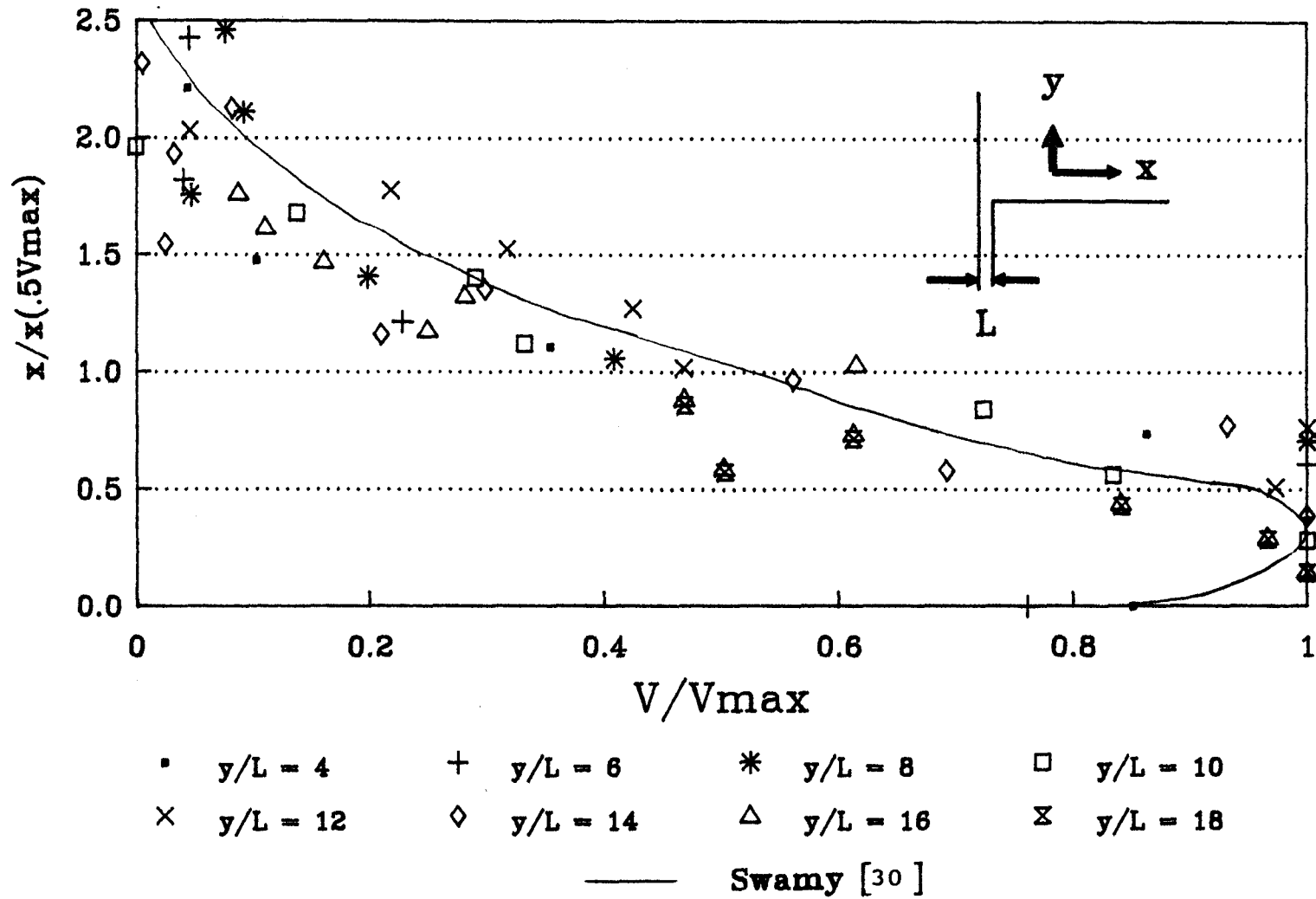
Figure 15 : Wall Jet Similarity Solution

## 6.1.2 Entire Cavity

The results from measurements gave a good indication of the recirculating flow present. For the low flow rate case studied (Re jet = 1167) two sets of measurements were obtained and as both are similar the results will be discussed together (Figure 16). The incoming jet is seen to diffuse and entrain fluid almost to the top of the cavity (to approximately 245 mm) where the effect of the upper boundary of the fluid can be seen and the flow turns toward the centre of the cavity. In the upper corner in the area where the main flow has turned from the upper wall a small area of recirculation (20 mm dia.) was observed. The flow then proceeds along the top surface before turning down the far wall. Again in the upper corner there is evidence of recirculation but on a much smaller scale than the opposite corner (approximately 10 mm dia.). The central core of the cavity is an area of large scale recirculation where the fluid velocity is much lower than the surrounding area. This area is slightly skewed towards the incoming jet side and this would be expected due to the preservation of continuity where the higher flow rate in a small area going up the cavity must equal the larger area lower flow rate going down the cavity. A disturbance caused

by the flow leaving the cavity was noted in the lower right side of the flow cavity. Unfortunately due to optical limitations the actual entry of the flow into the cavity could not be measured and as a result does not appear on the mean velocity plots.

1 mm = 9.5 mm/s      ▬ 1 cm
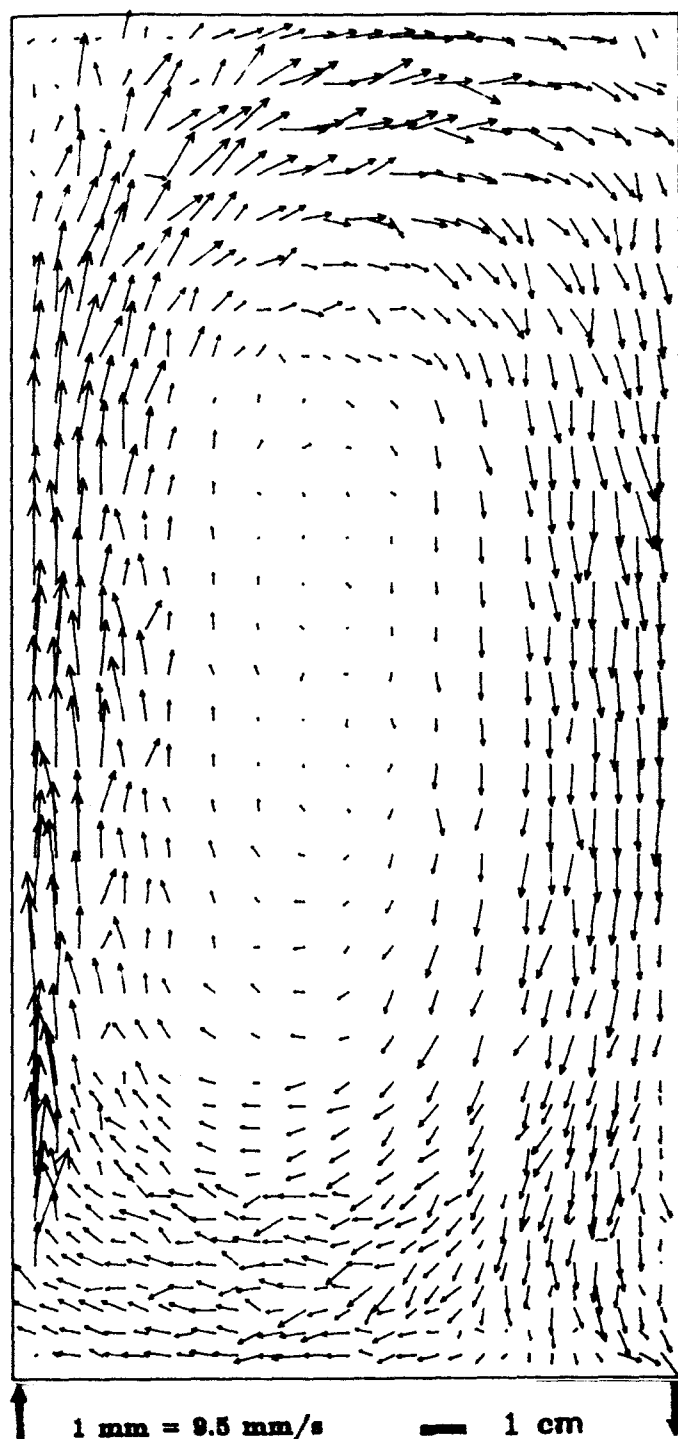
**Figure 16 : Mean Velocity Total Tank**
**Re nozzle = 1176**
**Experimental Data**

Plots of vertical velocity are shown at four heights in the cavity 60 mm, 125 mm, 185 mm, and 245 mm (Figures 17-20). At a cavity height of 60 mm the velocity gradient is seen to be very steep in the first 15 mm from the wall and the remaining velocities to be much lower. Proceeding up the cavity the velocity gradient gradually decreased as the wall jet fans out and loses momentum. Downcoming velocities are much lower at 60 mm than in the other cavity heights plotted. This is most likely due to the changing direction of the flow at 60 mm where it becomes more horizontal than vertical flow.

An analysis of the velocity profiles at each height revealed that continuity is satisfied at each cavity height with the difference between the upward flow and the downward flow to be not more than 7 % in the worst case.

(m/s)

TRAVERSE DISTANCE (cm)
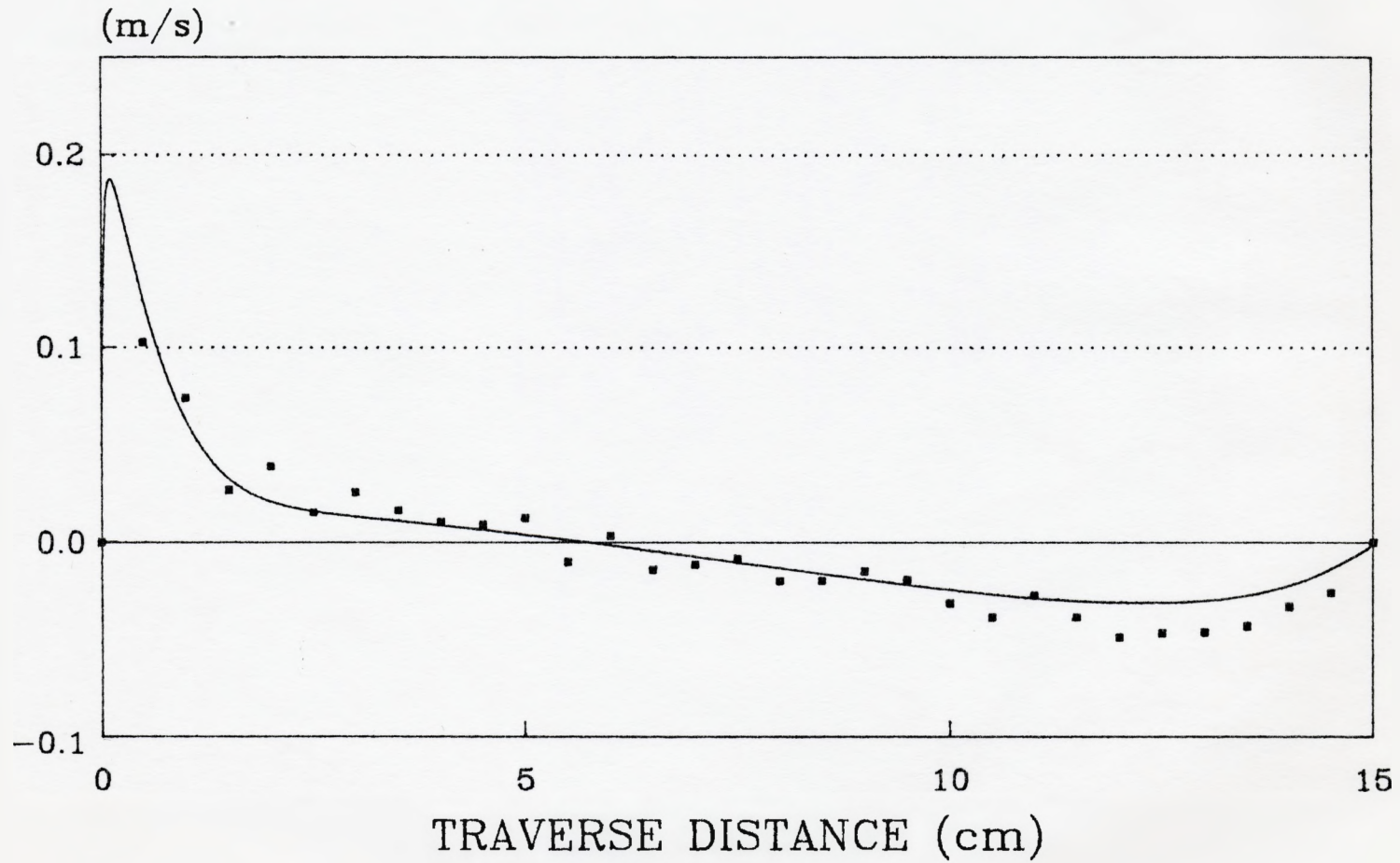
■  Experimental Data    ——  Numerical Results
**Figure 17 : Vertical Velocity**
**Tank Height 60 mm**
**Re nozzle = 1176**
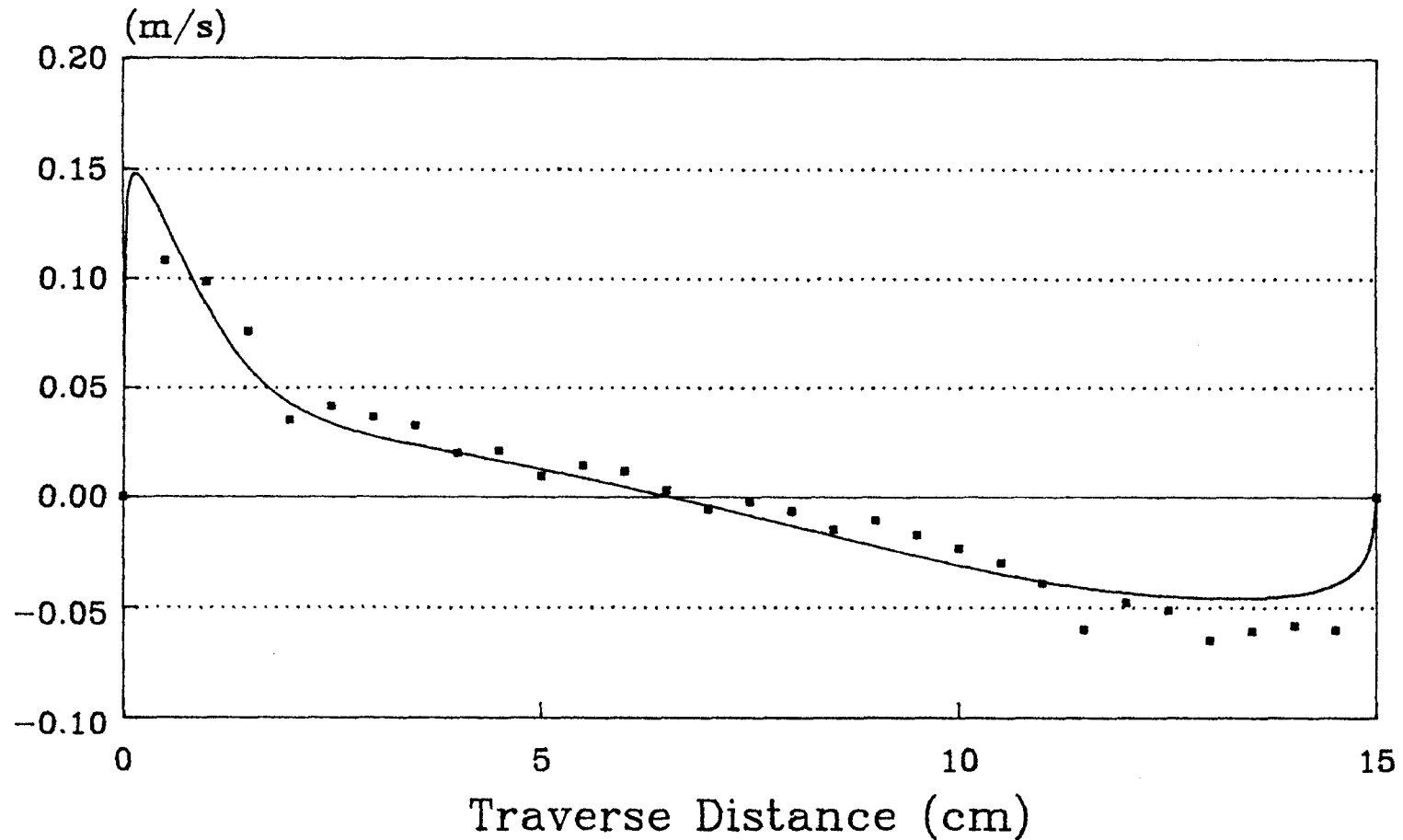
• Experimental Data ——— Numerical Results

**Figure 18 : Vertical Velocity**
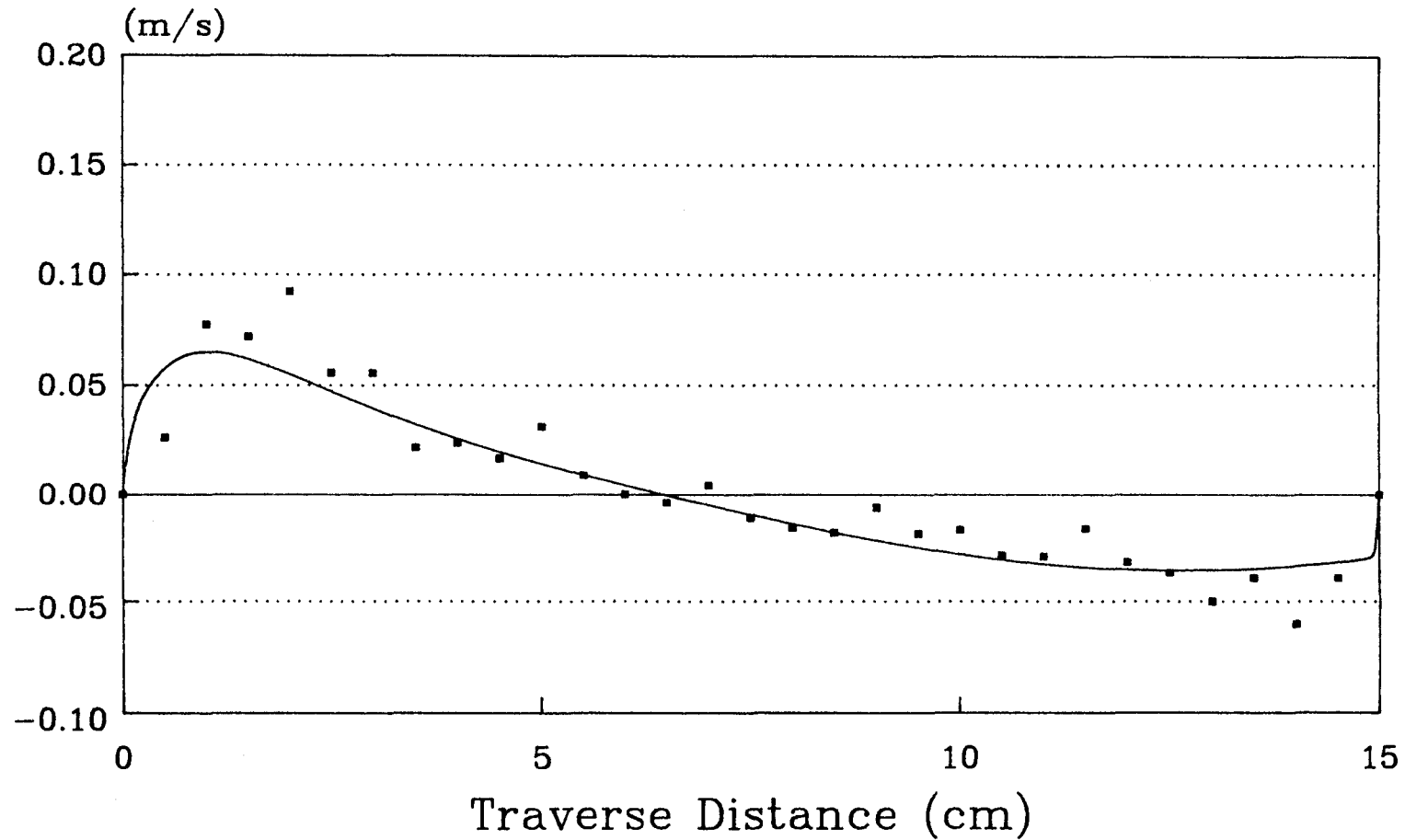
**Tank Height 125 mm**
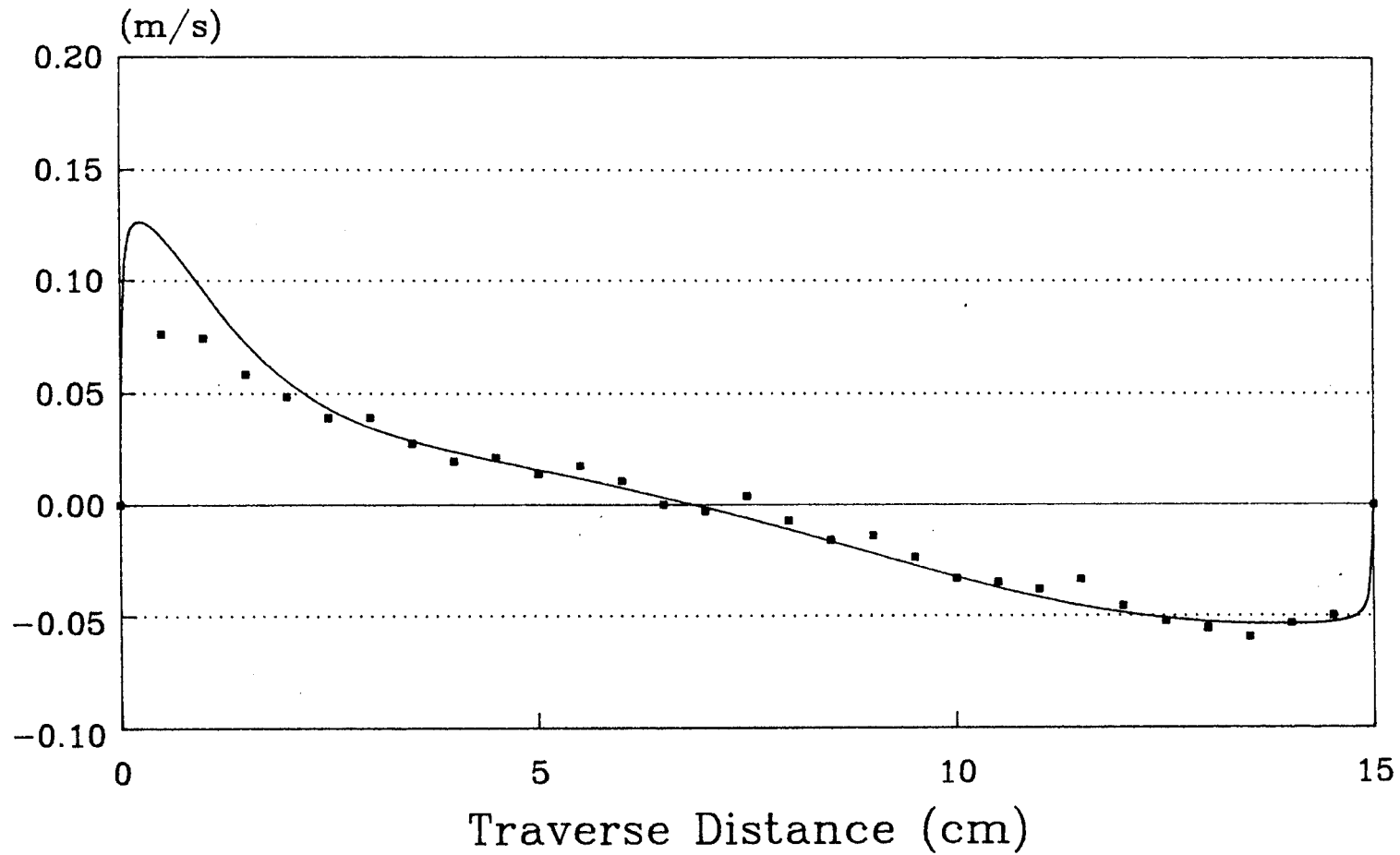
**Re nozzle = 1176**

Figure 19 : Vertical Velocity
Tank Height 185 mm
Re nozzle = 1176

Figure 20 : Vertical Velocity
Tank Height 245 mm
Re nozzle = 1176

Plots of turbulent kinetic energy ($0.5(\overline{u'}^2 + \overline{v'}^2)$) were plotted for the low flow rate case (Re jet = 1167) (Figure 21). The area of highest turbulent energy as seen on the plots is the incoming and diffusing jet area. The highest recorded value of turbulent energy was at a cavity height of 25 mm and 5 mm from the cavity wall and was 2.58E-3 m2/s2 which represents a turbulent intensity (based on the volume averaged incoming velocity) of 19.1 %. Also, most of the incoming jet train has a higher energy than the surrounding fluid right up to the top of the cavity. The central core of the cavity recorded the lowest values of turbulent energy (less than 4.5E-6 m2/s2) as was expected.

Plots of kinetic energy are shown at four heights in the cavity 60 mm, 125 mm, 185 mm, and 245 mm (Figures 22-25). At a cavity height of 60 mm the highest values of turbulent energy are seen in only the first 10 mm from the wall. At 125 mm a similar situation was observed although wider (25 mm from the wall) and of lower energy level. This is due to the energy of the jet losing momentum and spreading as it moves up the cavity. At 185 mm and 245 mm the peaks of energy are at the near wall region and are approximately 50 mm wide. Energy levels at these two heights are much lower than the incoming jet area.

It is interesting to note that turbulent energy
levels at the exit of the cavity are not large despite
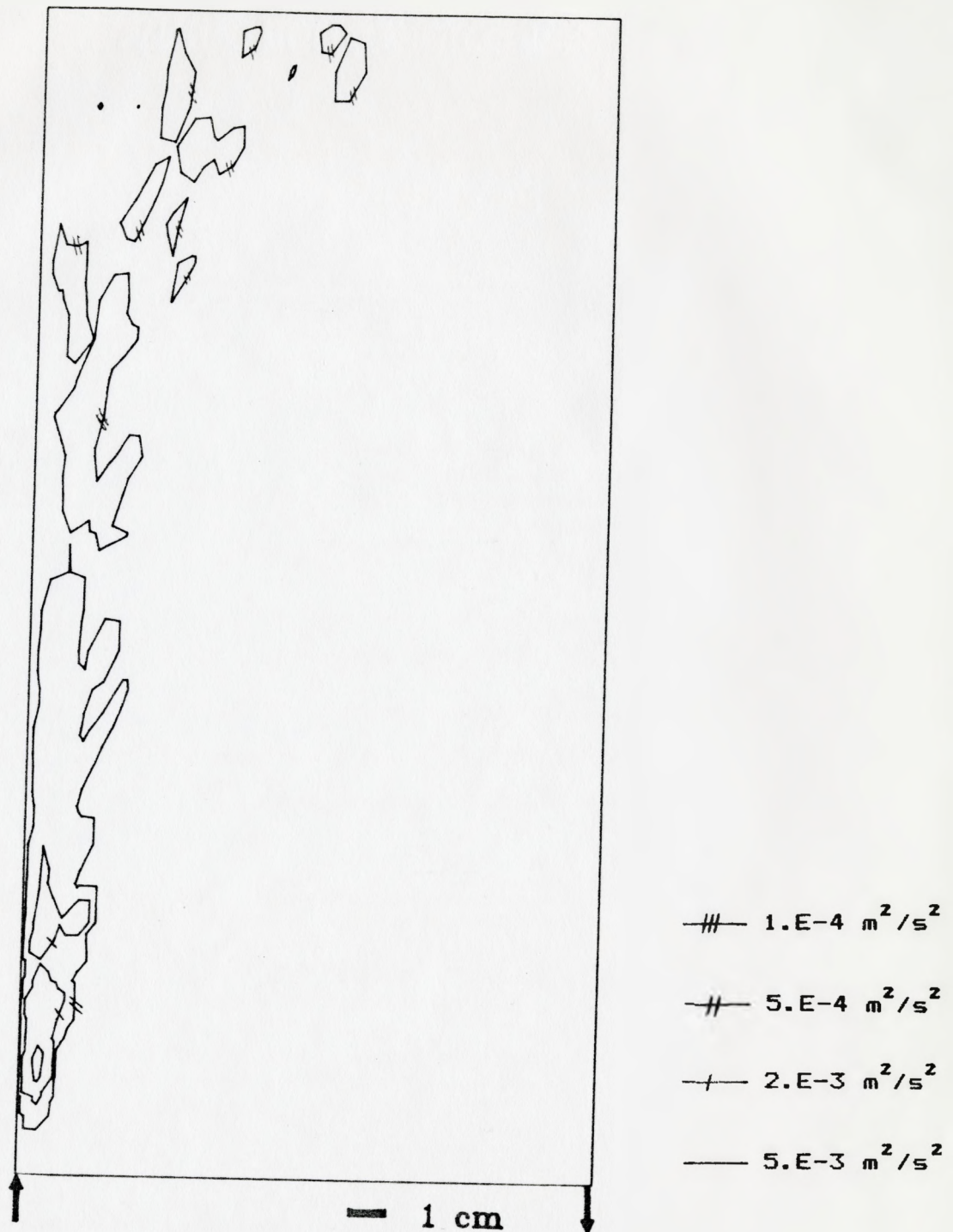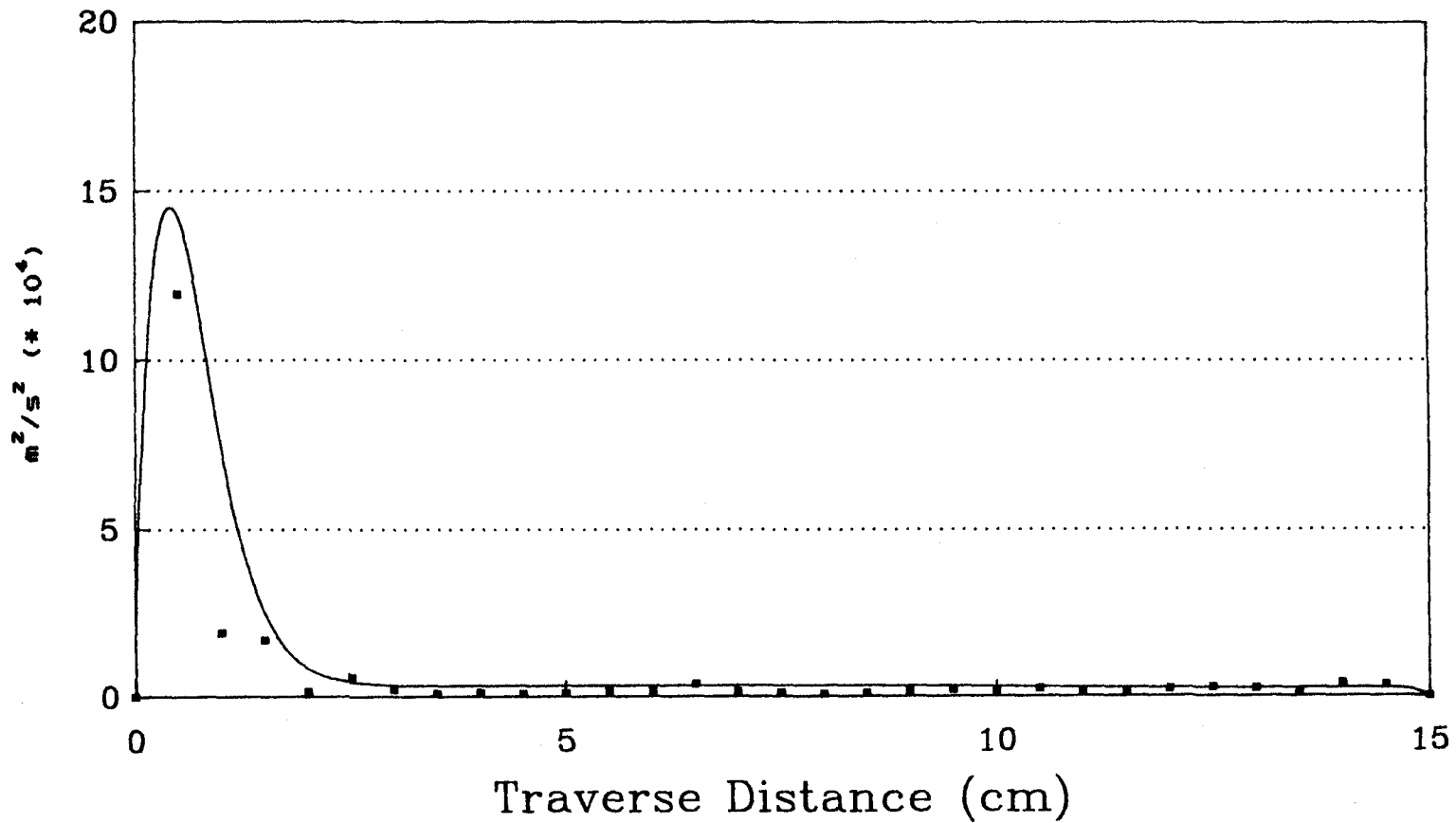the disruption in flow which occurs in that region.

Figure 21 : Turbulent Kinetic Energy
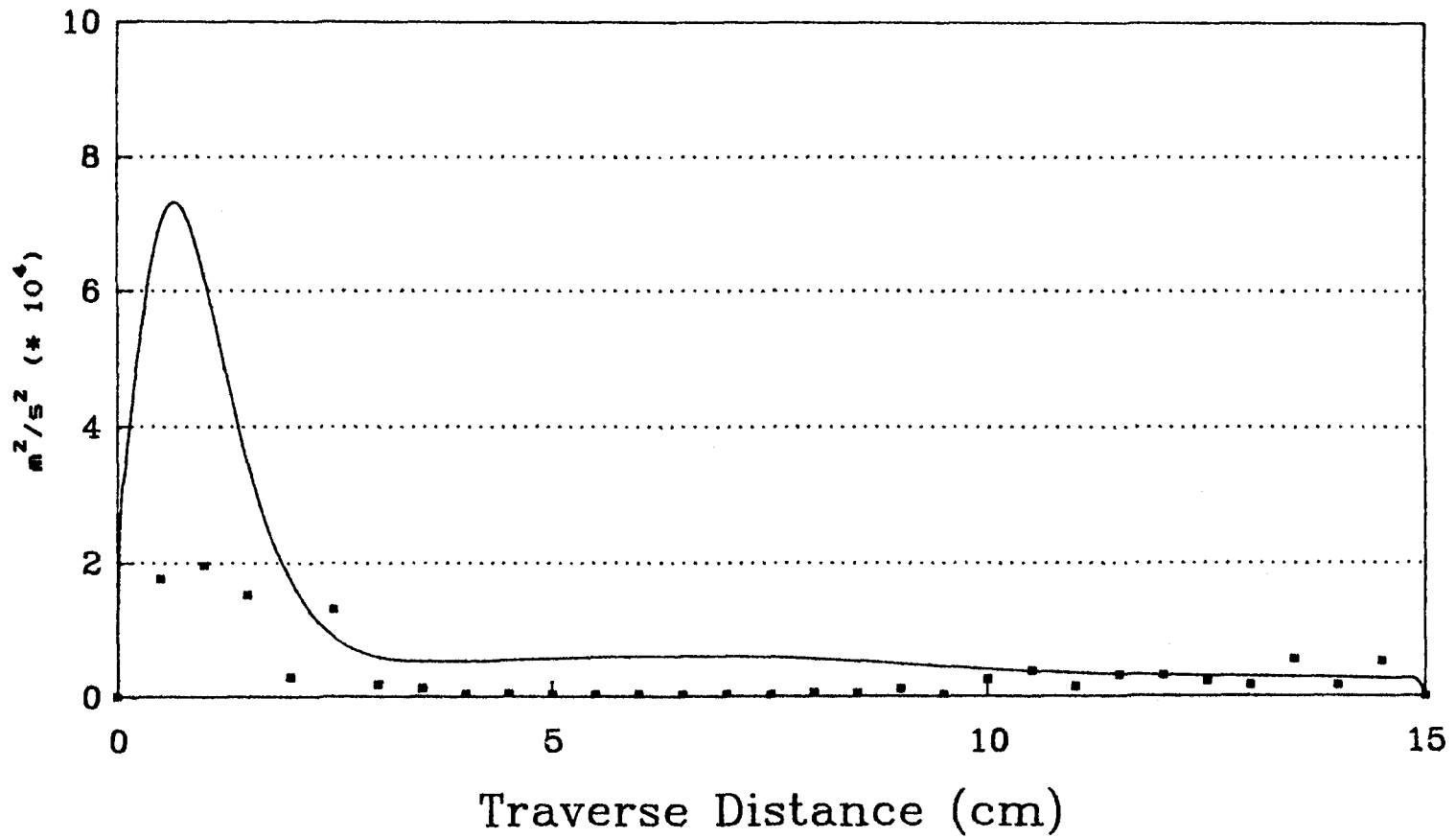Experimental Data
Re nozzle = 1176

Figure 22 : Turbulent Kinetic Energy
Tank Height 60 mm
Re nozzle = 1176

Figure 23 : Turbulent Kinetic Energy
Tank Height 125 mm
Re nozzle = 1176
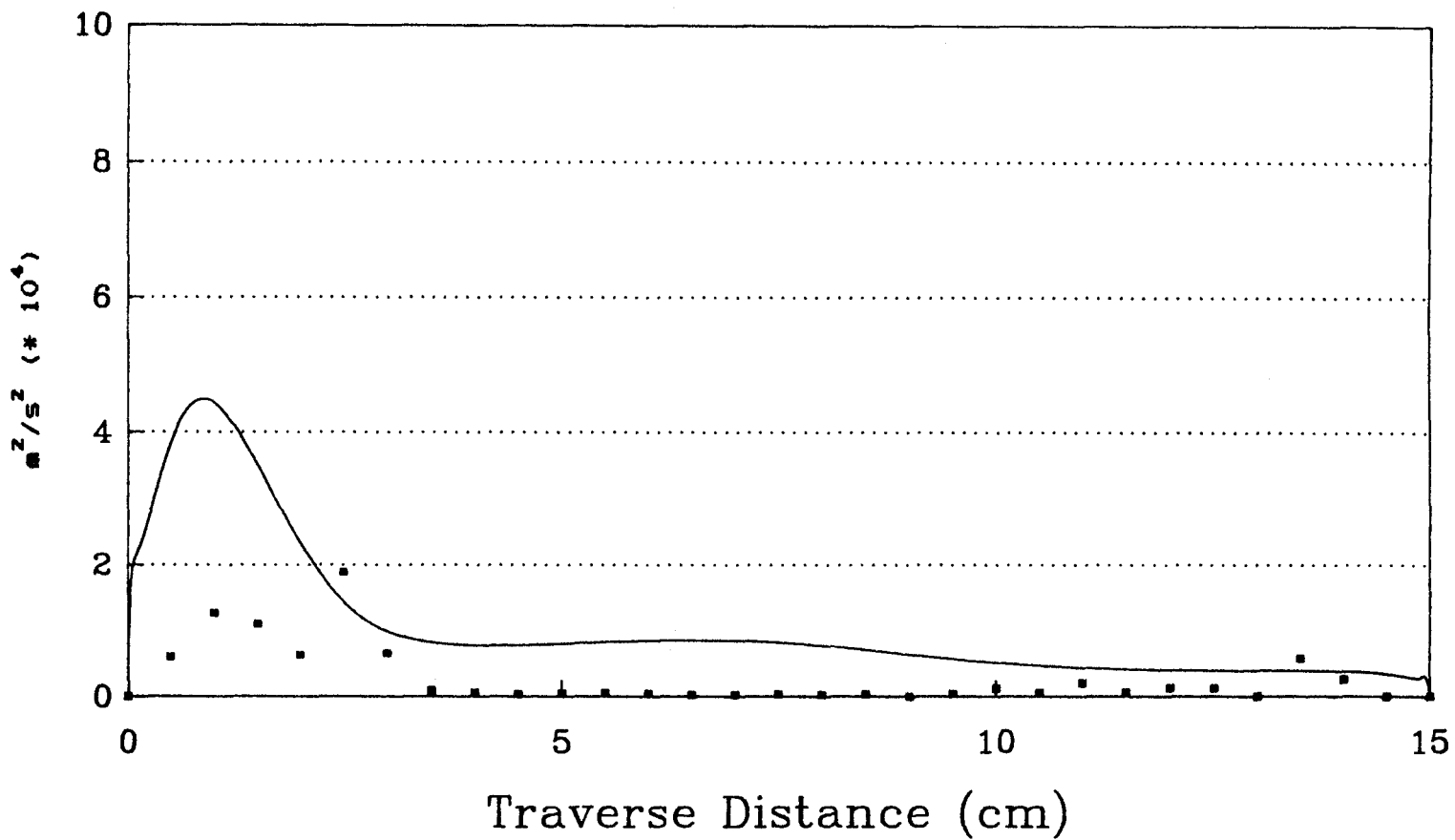
Figure 24 : Turbulent Kinetic Energy
Tank Height 185 mm
Re nozzle = 1176
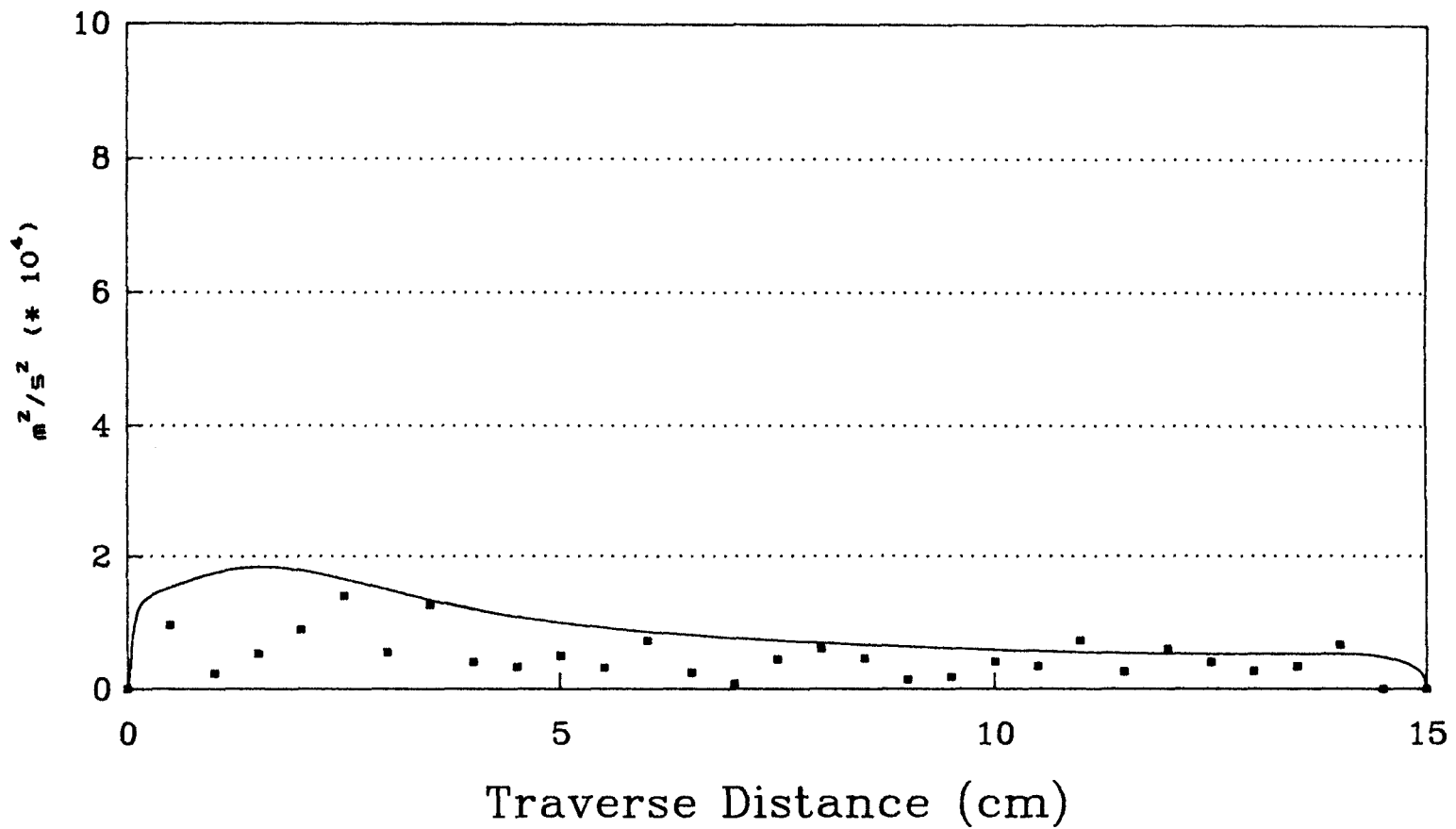
Figure 25 : Turbulent Kinetic Energy
Tank Height 245 mm
Re nozzle = 1176

For the higher flow rate case (Re jet = 3231) similar plots of velocity and kinetic energy were obtained (Figure 26). The mean velocity plot of the second case is similar in most respects to the first case discussed with some minor variations. The incoming jet is at a much higher velocity and therefore diffuses less up the side of the cavity. As a result, the large area of recirculation seen in the first case is much smaller here as the flow does not curve toward the top or become unattached from the wall. The small area of recirculation seen in the other top corner is present in this case and is of approximately the same size.

Plots of vertical velocity are shown at four heights in the cavity 60 mm, 120 mm, 180 mm, and 240 mm (Figures 27-30). At a cavity height of 60 mm the velocity gradient is seen to be very steep in the first 10 mm from the wall and the remaining velocities to be much lower. The gradient is steeper than that found in the lower flow rate case and this is to be expected due to the higher energy jet losing less momentum going up the cavity. In other respects the vertical velocity plots are similar.

1 mm = 16.5 mm/s          ▬ 1 cm
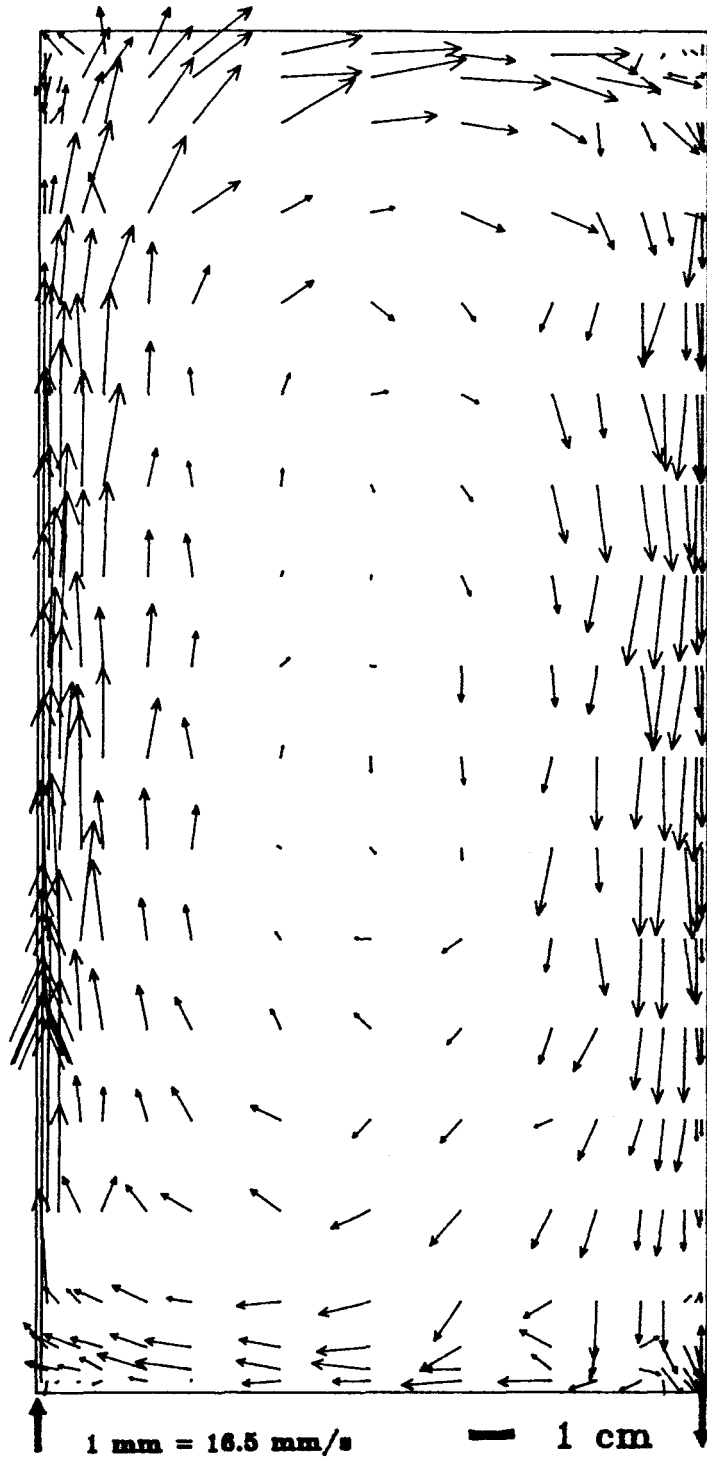
Figure 26 : Mean Velocity Total Tank
Re nozzle = 3231
Experimental Data
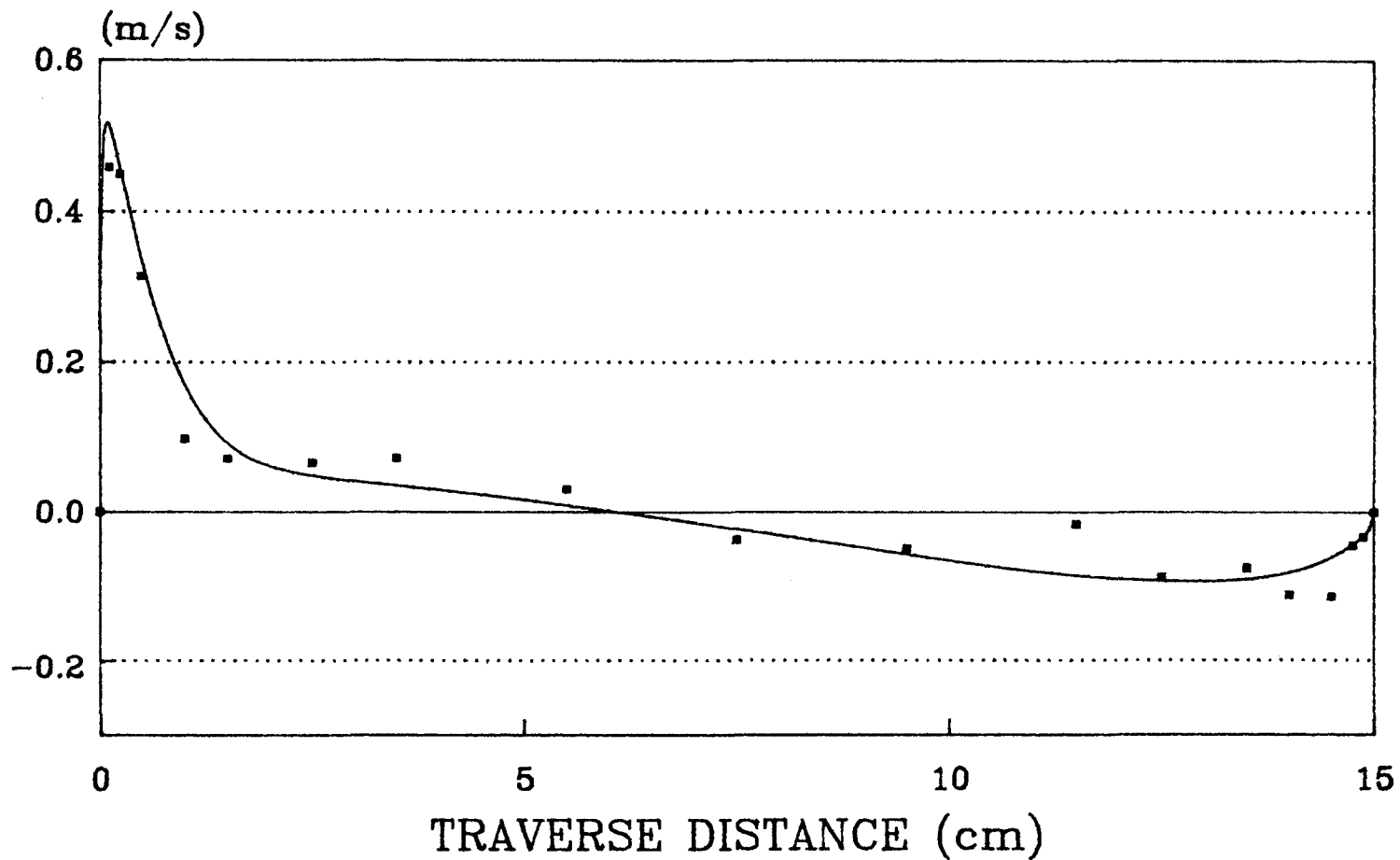
Figure 27 : Vertical Velocity
Tank Height 60 mm
Re nozzle = 3231
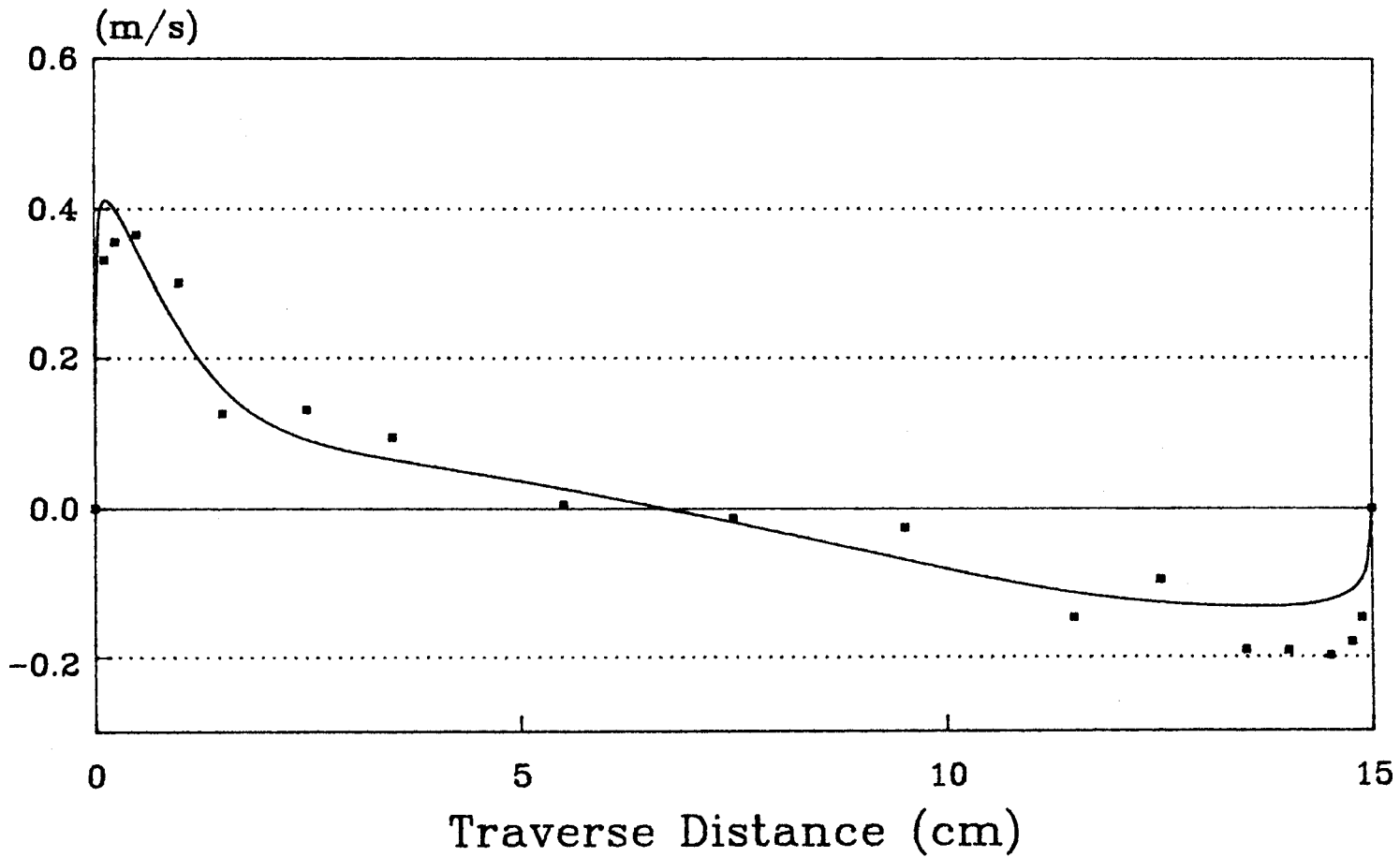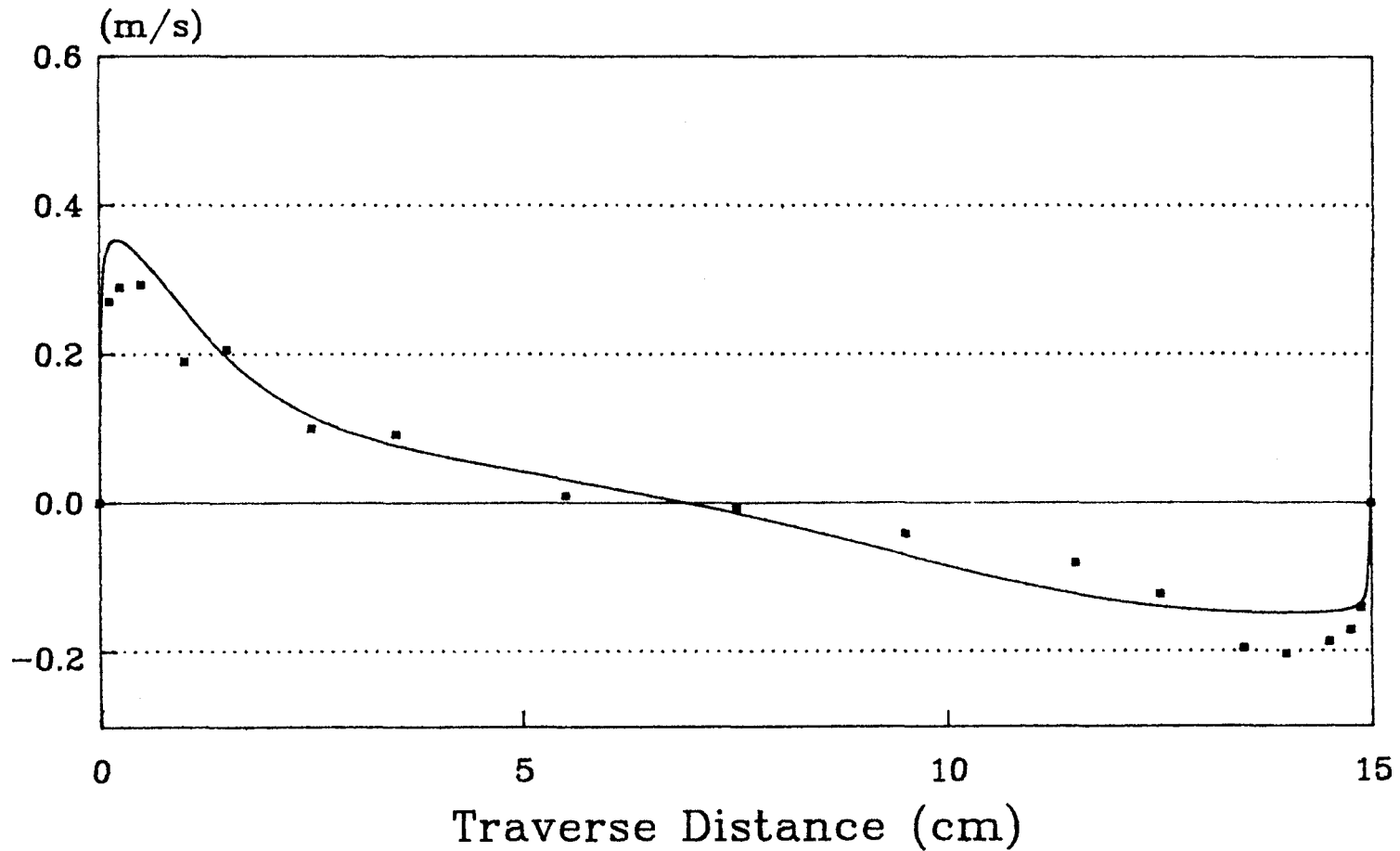
■ Experimental Data ——— Numerical Results

Figure 28 : Vertical Velocity
Tank Height 120 mm
Re nozzle = 3231

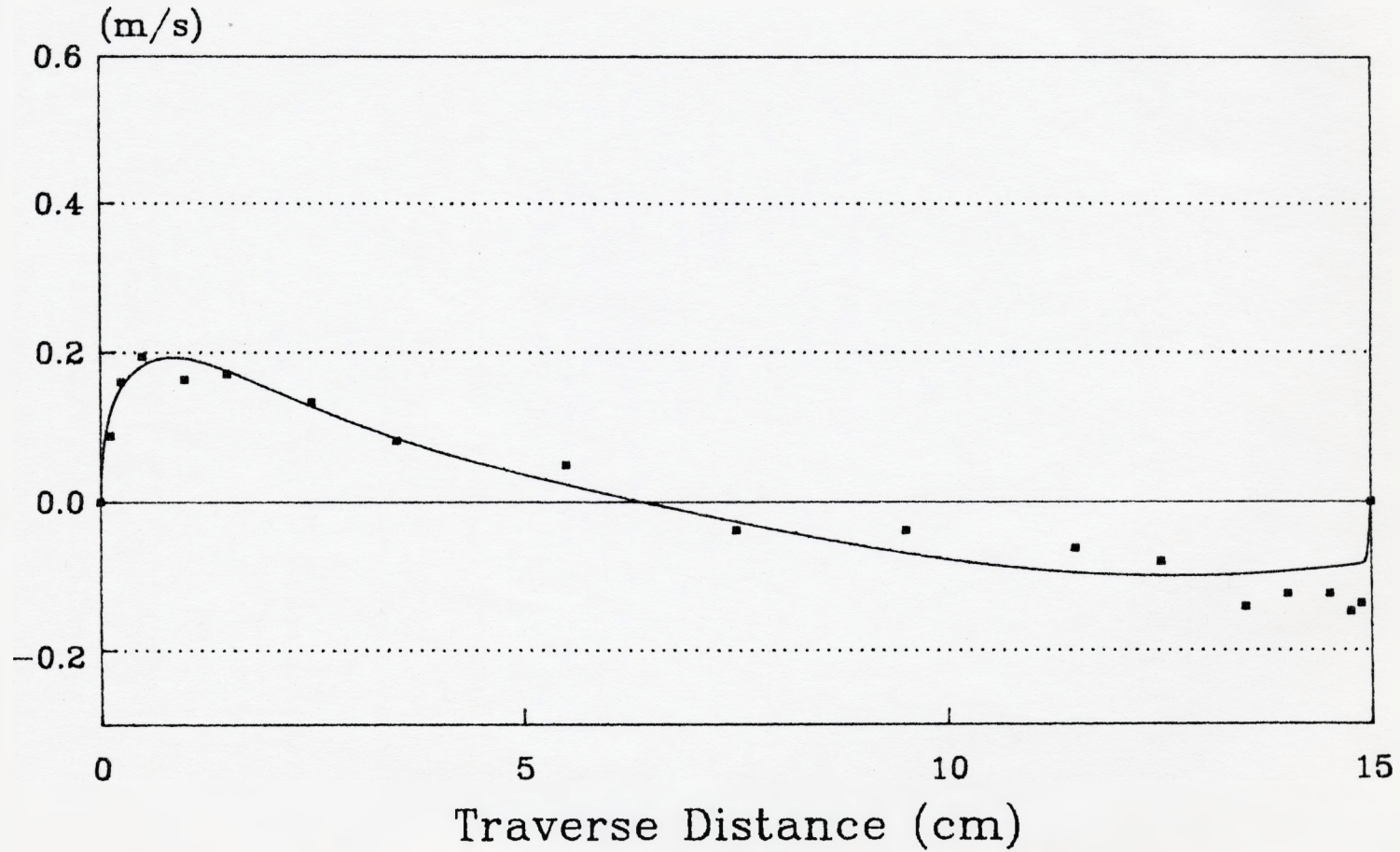■ Experimental Data ——— Numerical Results

Figure 29 : Vertical Velocity
Tank Height 180 mm
Re nozzle = 3231

Figure 30 : Vertical Velocity
Tank Height 240 mm
Re nozzle = 3231

Plots of turbulent kinetic energy ($0.5(\overline{u'}^2 + \overline{v'}^2)$) were also plotted for the high flow rate case (Re jet = 3231) (Figure 31). The area of highest turbulent energy as seen on the plots is the incoming and diffusing jet area. The highest recorded value of turbulent energy was at a cavity height of 25 mm and 5 mm from the cavity wall and was 1.30E-2 m2/s2 which represents a turbulent intensity (based on the volume averaged incoming velocity) of 15.8 %. Also, most of the incoming jet train has a higher energy than the surrounding fluid right up to the top of the cavity. The central core of the cavity recorded the lowest values of turbulent energy (less than 5E-4 m2/s2) as was expected.

Plots of kinetic energy are shown at four heights in the cavity 60 mm, 120 mm, 180 mm, and 240 mm (Figures 32-35). At a cavity height of 60 mm the turbulent kinetic energy near the walls was very high and fluctuating. At 120 mm, 180 mm and 240 mm the peaks of energy are at the near wall region and are approximately 25 mm wide. Energy levels at these heights are much lower than the incoming jet area.

Again it is interesting to note that turbulent energy levels at the exit of the cavity are not large despite the disruption in flow which occurs in that region.

—#— 5.E-4 m²/s²

—#— 5.E-3 m²/s²

—+— 2.E-2 m²/s²

——— 4.E-2 m²/s²

■ 1 cm
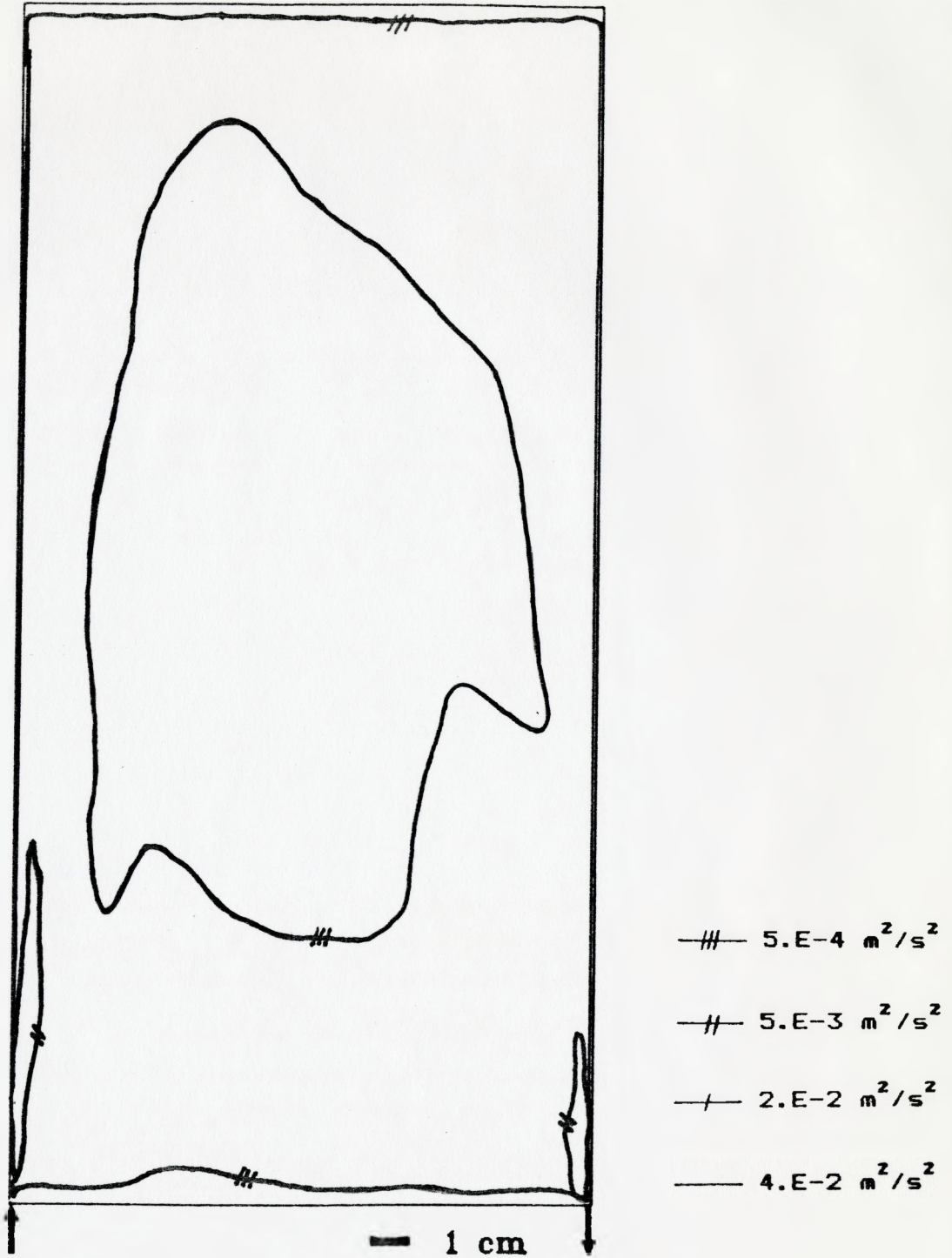
Figure 31 : Turbulent Kinetic Energy
Experimental Data
Re nozzle = 3231
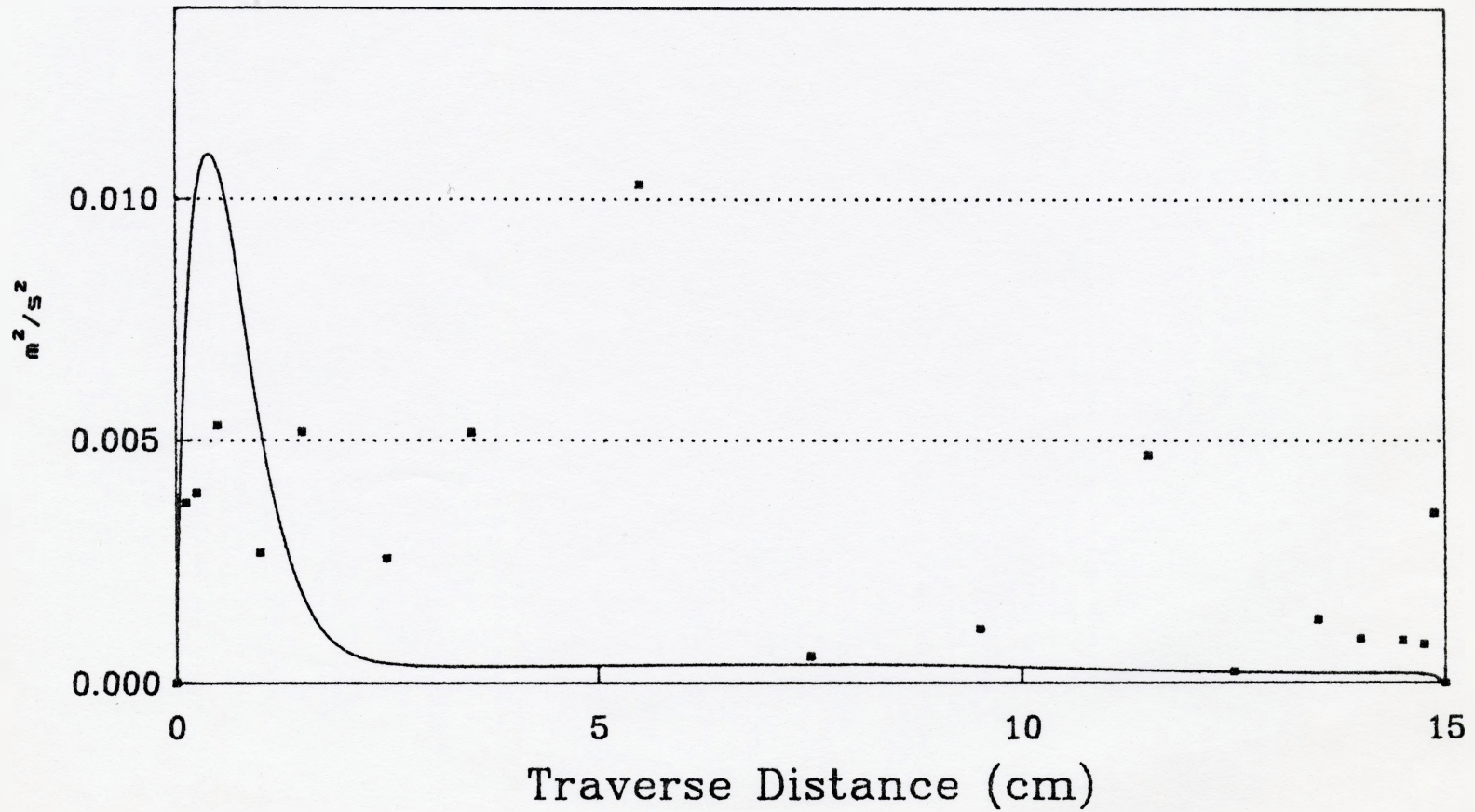
Figure 32 : Turbulent Kinetic Energy
Tank Height 60 mm
Re nozzle = 3231
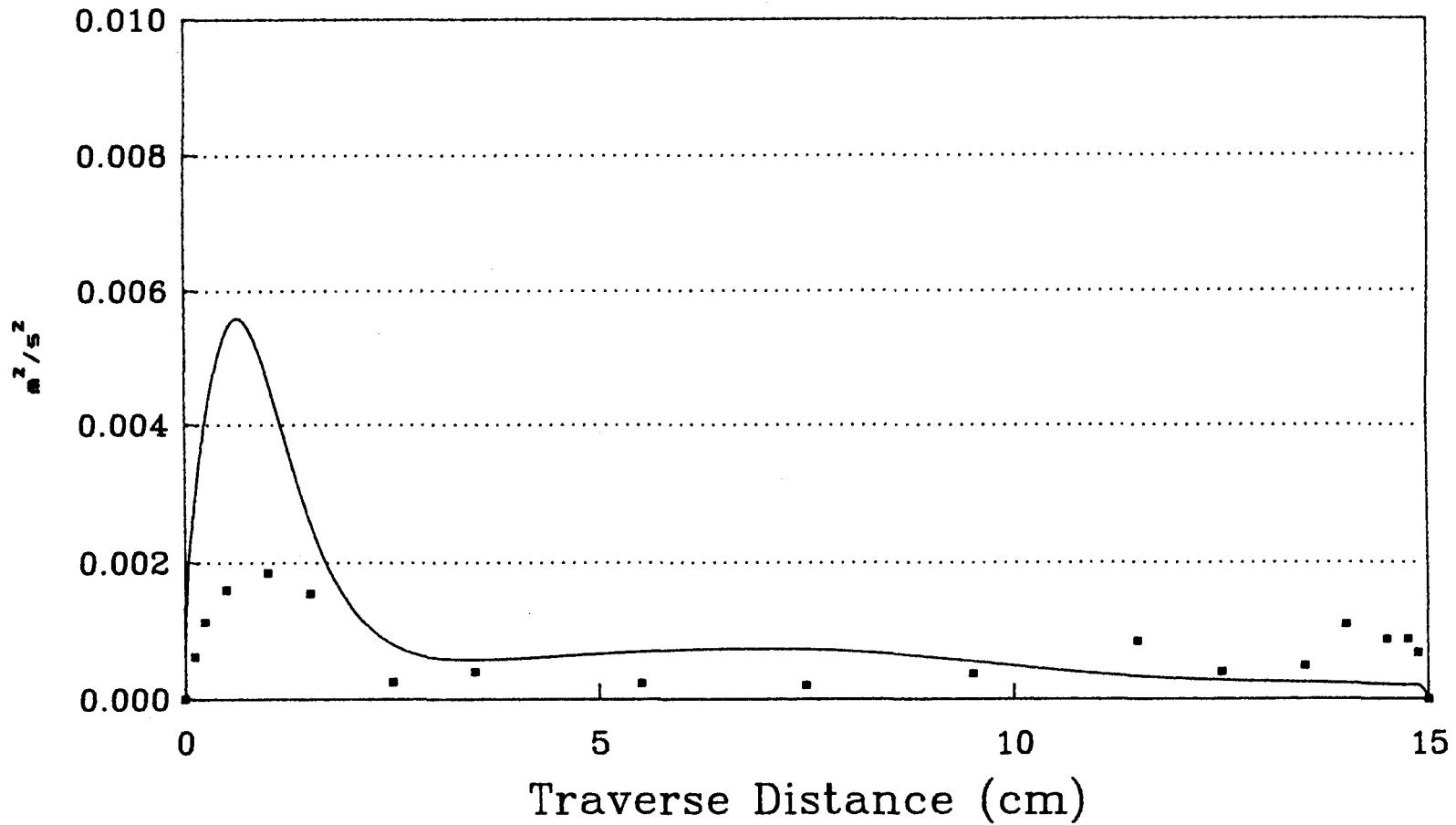
Figure 33 : Turbulent Kinetic Energy
Tank Height 120 mm
Re nozzle = 3231
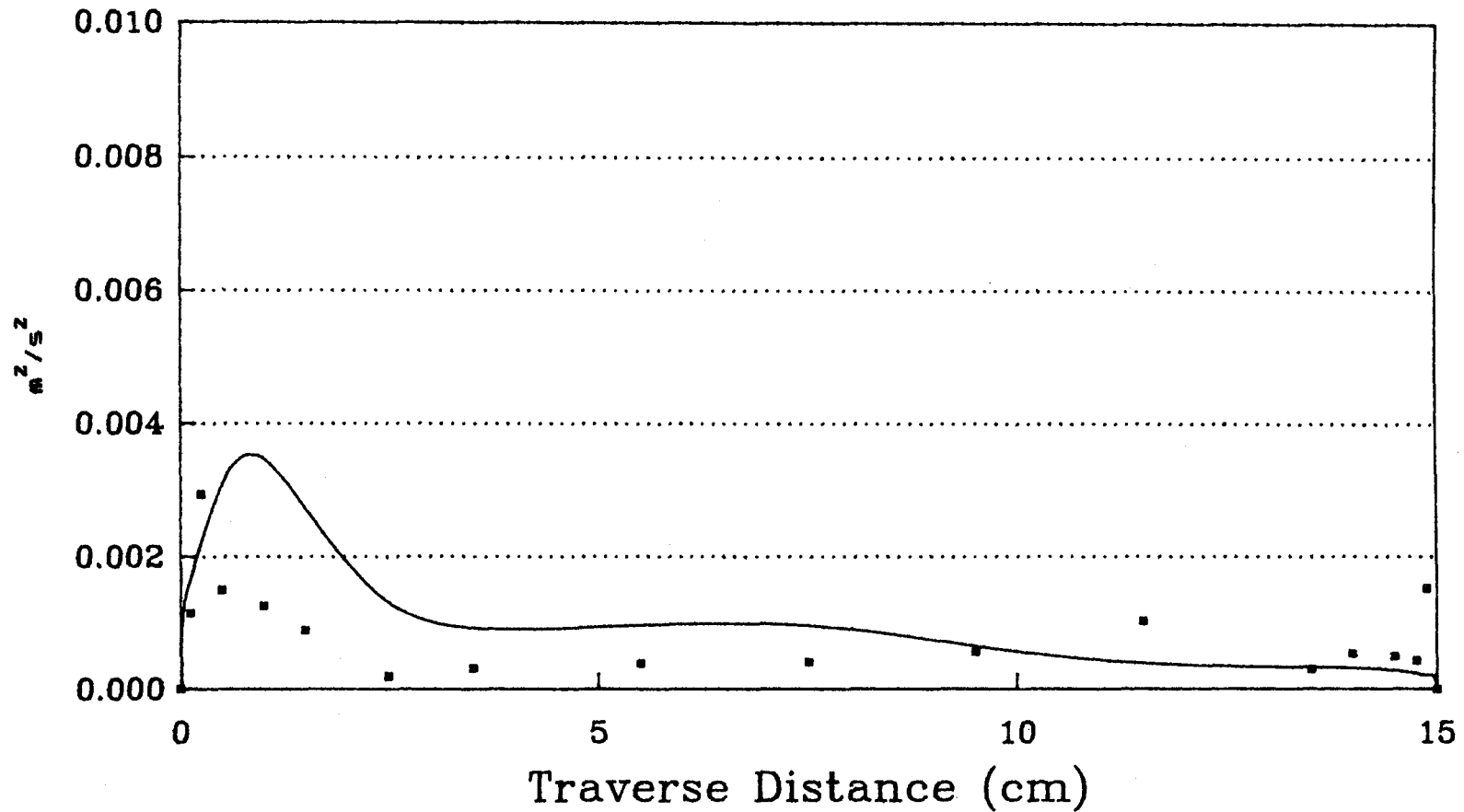
Figure 34 : Turbulent Kinetic Energy
Tank Height 180 mm
Re nozzle = 3231
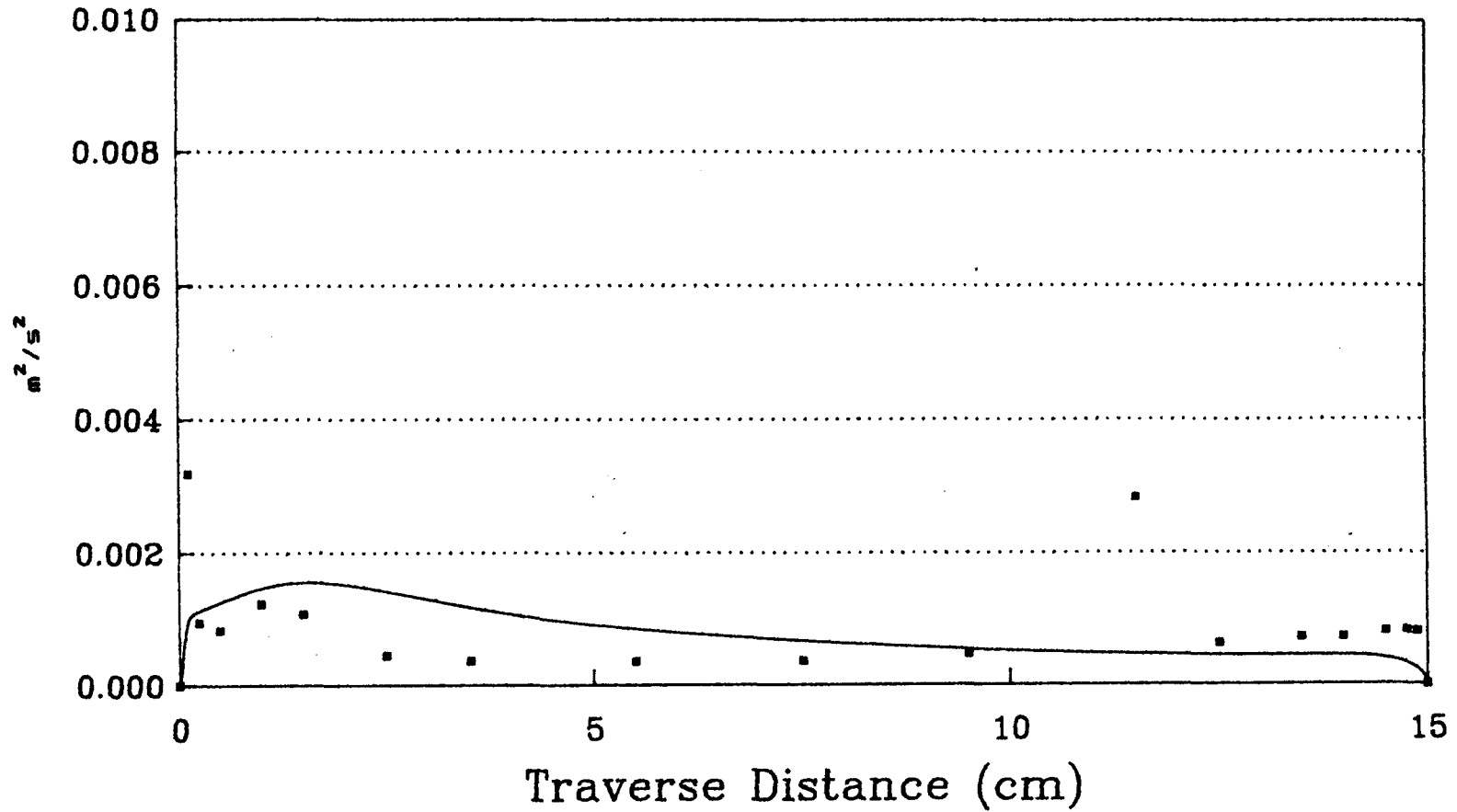
Figure 35 : Turbulent Kinetic Energy
Tank Height 240 mm
Re nozzle = 3231

- Experimental Data    ——— Numerical Results

## 6.2 NUMERICAL RESULTS

Numerical Results are presented for both flow cases under study and they are quite similar to the experimental measurements and will be discussed now.

The numerical results gave a good indication of the recirculating flow experimentally measured (Figure 36). Similar to the experimental results the incoming jet is seen to diffuse and entrain fluid almost to the top of the cavity (to approximately 245 mm) where the effect of the upper boundary of the fluid can be seen and the flow turns toward the centre of the cavity. In the upper corner in the area where the main flow has turned from the upper wall a small area of recirculation (20 mm dia.) was observed. The flow then proceeds along the top surface before turning down the far wall. Again in the upper corner there is evidence of recirculation but on a much smaller scale than the opposite corner (approximately 10 mm dia.). The central core of the cavity is an area of large scale recirculation where the fluid velocity is much lower than the surrounding area. This area is slightly skewed towards the incoming jet side and this would be expected due to the preservation of continuity where the higher flow rate in a small area going up the cavity must equal the larger area lower

flow rate going down the cavity. A disturbance caused by the flow leaving the cavity was noted in the lower right side of the flow cavity. The actual entry of the jet into the cavity although not measured experimentally appears on the computational mean velocity plots.

1 mm = 8.5 mm/s ━━ 1 cm
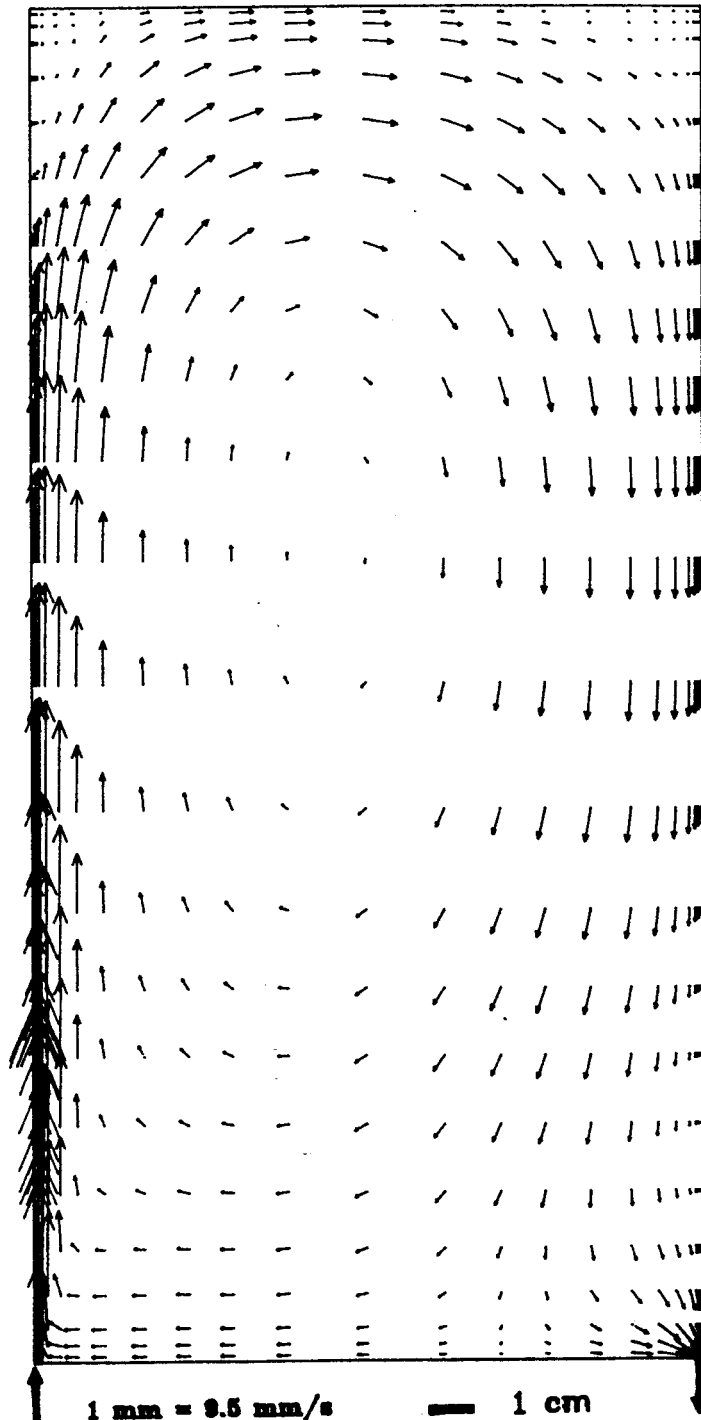
**Figure 36 : Mean Velocity Total Tank
Computational Results
Re nozzle = 1176**

Plots of turbulent kinetic energy were plotted for the low flow rate case (Re jet = 1167) (Figure 37). The area of highest turbulent energy as seen on the plots is the incoming and diffusing jet area. The highest computed value of turbulent energy was at a cavity height of 15 mm and 3 mm from the cavity wall and was 6.147E-3 m2/s2 which represents a turbulent intensity (based on the volume averaged incoming velocity) of 29.4 %. Also, most of the incoming jet train has a higher energy than the surrounding fluid right up to the top of the cavity. The central core of the cavity recorded the lowest values of turbulent energy (less than 1.0E-5 m2/s2) as was expected.

Plots of turbulent kinetic energy are shown at four heights in the cavity 60 mm, 125 mm, 185 mm, and 245 mm (Figures 21-24). At a cavity height of 60 mm the highest values of turbulent energy are seen in only the first 10 mm from the wall. At 125 mm a similar situation was observed although wider (25 mm from the wall) and of lower energy level. This is due to the energy of the jet losing momentum and spreading as it moves up the cavity. At 185 mm and 245 mm the peaks of energy are at the near wall region and are approximately 50 mm wide. Energy levels at these two heights are much lower than the incoming jet area.

The turbulent energy levels at the exit of the cavity are large enough to appear on the turbulent kinetic energy plot for the whole cavity although are at a much lower level (1E-4 m2/s2) than the incoming turbulent energies.

$1.E-4 \ m^2/s^2$

$5.E-4 \ m^2/s^2$

$2.E-3 \ m^2/s^2$

$5.E-3 \ m^2/s^2$

1 cm
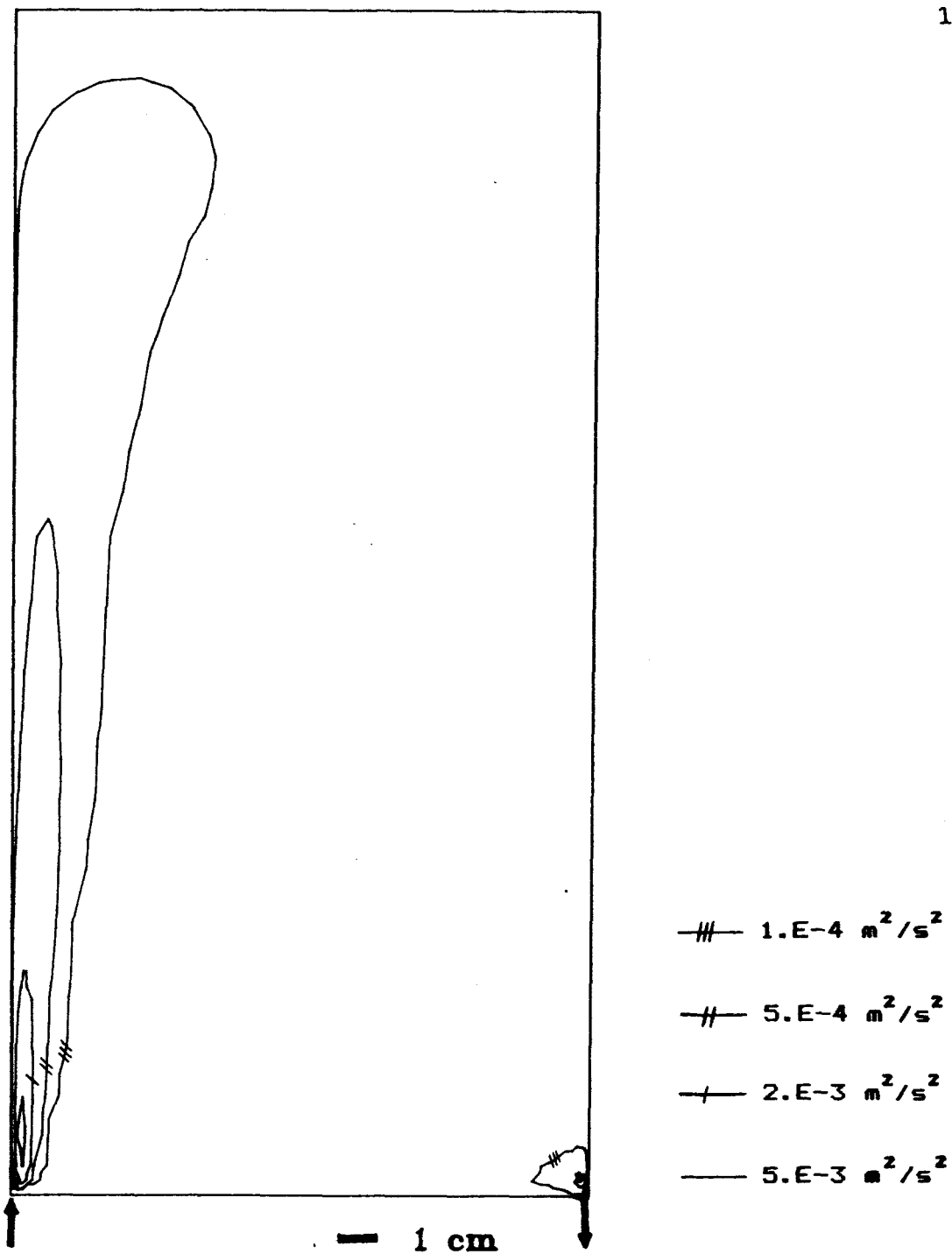
Figure 37 : Turbulent Kinetic Energy
Computational Results
Re nozzle = 1176

For the higher flow rate case (Re jet = 3231) similar plots of velocity and kinetic energy were obtained. The mean velocity plot of the second case is similar in most respects to the first case discussed with some minor variations (Figure 38). The incoming jet is at a much higher speed and therefore diffuses less up the side of the cavity. As a result, the large area of recirculation seen in the first case is much smaller here as the flow does not curve toward the top or become unattached from the wall. The small area of recirculation seen in the other top corner is present in this case and is of approximately the same size.

1 mm = 16.5 mm/s        ▬ 1 cm
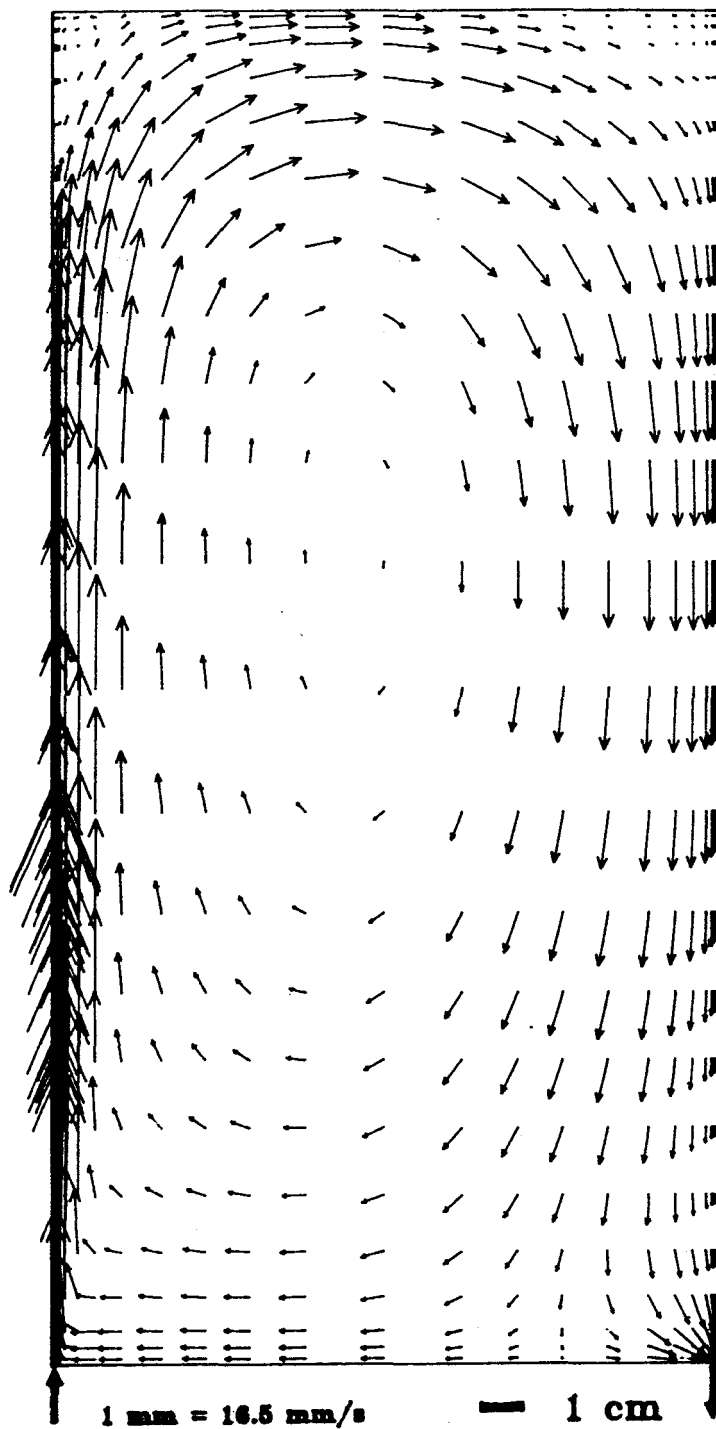
**Figure 38 : Mean Velocity Total Tank
Computational Results
Re nozzle = 3231**

Plots of turbulent kinetic energy were also plotted for the high flow rate case (Re jet = 3231) (Figure 39). The area of highest turbulent energy as seen on the plots is the incoming and diffusing jet area. The highest recorded value of turbulent energy was at a cavity height of 15 mm and 3 mm from the cavity wall and was 4.465E-2 m2/s2 which represents a turbulent intensity (based on the volume averaged incoming velocity) of 29.5 %. Also, most of the incoming jet train has a higher energy than the surrounding fluid right up to the top of the cavity. The central core of the cavity recorded the lowest values of turbulent energy (less than 1E-3 m2/s2) as was expected.

Turbulent energy levels at the exit of the cavity are not large despite the disruption in flow which occurs in that region (less than 5E-3 m2/s2).

—#— 5.E−4 $m^2/s^2$

—#— 5.E−3 $m^2/s^2$

—+— 2.E−2 $m^2/s^2$

——— 4.E−2 $m^2/s^2$

▬ 1 cm
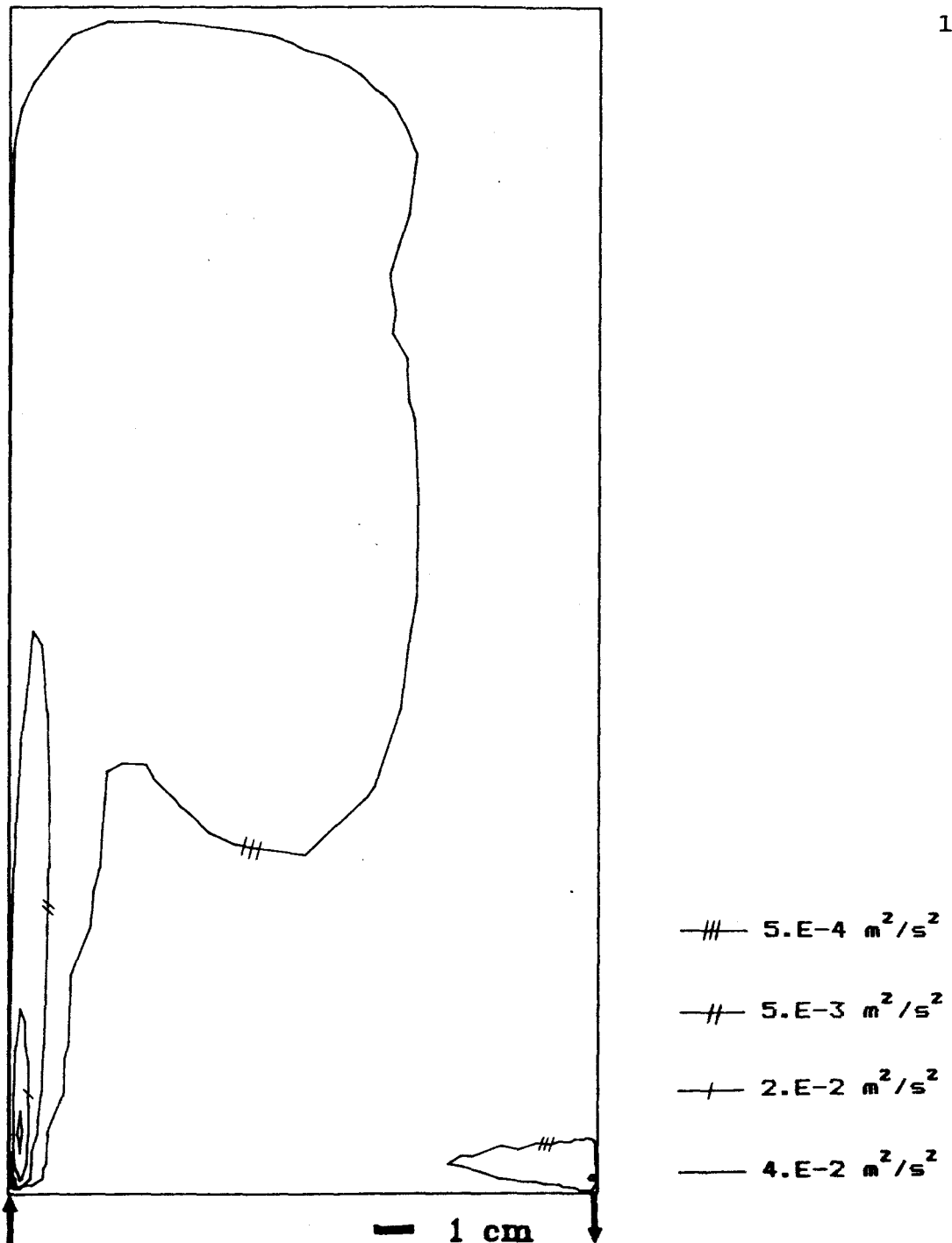
**Figure 39 : Turbulent Kinetic Energy
Computational Results
Re nozzle = 3231**

# 6.3 COMPARISON OF EXPERIMENTAL DATA AND NUMERICAL RESULTS

## 6.3.1 Velocity Plots

For the lower flow case (Re jet = 1167) excellent agreement is obtained between the mean velocity plots (see Figures 16, 17-20, and 36). The computer code predicts the areas of recirculation in the upper corners of the cavity and predicts the same size scale of recirculation. The upper left hand area is a approximately twice the size of the area of recirculation in the upper right hand corner as was found to be true in the experimental investigation. Referring to the plots of vertical velocity at four cavity heights (Figures 17-20), the agreement between the code and experimental measurements is further reinforced. At a cavity height of 60 mm (Figure 17) the experimental points fall on the curve of the numerical results with very good agreement. Due to optical limitations it was not possible to capture the peak of the incoming jet profile near the wall experimentally but all other points measured give excellent agreement. At 125 mm, 185 mm, and 245 mm the numerical results again give excellent agreement with the measured values (Figures 18 - 20). Both experimental data and

numerical results show a loss in momentum of the incoming jet as it flows up the cavity wall. At 245 mm the flow measured was higher than the numerical results in the first 5 cm of traverse distance (Figure 20). This result could be due to three dimensional effects of the wall jet impinging on the upper surface of the cavity.

For the higher flow case (Re jet = 3231) excellent agreement is again obtained between the mean velocity plots (see Figures 26, 27 - 30, and 38). The computer code predicts the areas of recirculation in the upper corners of the cavity and predicts the same size scale of recirculation. The upper left hand area is approximately twice the size of the area of recirculation in the upper right hand corner as was found to be true in the lower flow rate case. Referring to the plots of vertical velocity at four cavity heights (Figures 27 - 30), the agreement between the code and experimental measurements is again seen. At a cavity height of 60 mm (Figure 27) the experimental points fall on the curve of the numerical results with very good agreement. At 120 mm, 180 mm, and 240 mm (Figures 28- 30) the numerical results again give excellent agreement with the measured values with the exception of under- prediction of the downward flow near the wall. Both

to the lower flow rate case. At 120 mm and 180 mm (Figures 33, 34) although the profiles are similar the code predicts somewhat higher turbulent kinetic energy at the diffusing jet area than that which was measured experimentally. At 240 mm (Figure 35) the numerical results again give good agreement with the measured values.

The agreement obtained between the experimental data and the numerical results in the kinetic energy cases is much better than that previously obtained by others such as Boyle and Golay [14]. Few researchers include the results of kinetic energy comparisons due to the lack of agreement between experimental data and numerical results.

# CHAPTER SEVEN

## DISCUSSION AND CONCLUSIONS

Analysis of the available literature showed that recirculating flow within a cavity has received very little attention in the past and that very seldom has computational work been presented in good agreement with recirculating flow measurements. This study has attempted to rectify both of the above situations.

The use of the Laser Doppler Anemometer in the experimental portion of the study allowed very detailed flow pattern measurements to be made of instantaneous velocity where other methods could never be used in an enclosed cavity. The data collection of both mean velocities and fluctuating components allowed turbulent kinetic energies to be obtained without disturbing the flow. Velocity vector plots and turbulent kinetic energy plots provided visual representation of the flow present.

The computational results simulated the experimental work very well. The velocity plots gave excellent agreement with the experimental measurements in both magnitude and flow pattern presented. The turbulent kinetic energy results also gave good

predictions although the code somewhat overpredicted the peak magnitude in some cases. The comparison demonstrated that the k - $\epsilon$ model is capable of predicting isothermal recirculating flows.

The use of LDA in the experimental study complemented by the accurate computational analysis allowed a complete picture of recirculating flow in a cavity to be presented.

## CHAPTER EIGHT

## RECOMMENDATIONS AND FUTURE WORK

In order to ascertain the general applicability of the present computational form of the $k - \epsilon$ turbulence model other geometries could be studied such as the square cavity or cylindrical vessel. Other variations could include a change in inlet orifice or a repositioning of the jet to the centre of the cavity bottom with two exit jets at the bottom sides which would experimentally model the CANDU calandria studies of Ahluwalia and Shoukri [28]. As well, the examination of mixed convective flows such as a wall jet and an opposing heated wall would be a useful study for comparison purposes.

# APPENDIX A

## OPTICAL PROPERTIES

Laser        Power >5 mW           Wavelength 632.8 nm

        Beam dia. 0.8 mm at 1/e2 points

Focusing Lens (TSI 918)

    Fd = 243 mm     Phi = 11.52°   50 mm beam separation


Fringe spacing

    $df = 1/(2 \sin (Phi/2))$

      $= 632.8E{-}9/(2\sin(11.52/2))$

      $= 3.15E{-}6$ m

Apparent Focal Length (corrected for tank material and water)

    d = 220 mm      t = 6 mm

     2 = 1.48 (plexiglas)

     3 = 1.32 (water)

Phi a = 8.72 deg.

Theta 1 = 5.76 deg.

     2 = 3.89 deg.

     3 = 4.36 deg.

Apparent Fd =

        = 251.08 mm (apparent)

# APPENDIX B

## LDA APPARATUS

Laser        Spectra Physics Model 120 He Ne 5 mW

             Spectra Physics Laser Exciter

Optics

Transmitting

             TSI Model 902 Polarization Rotator

                TSI Model 915 Beamsplitter

             TSI Model 982 Bragg Cell Optical Module

             TSI Model 918 Focussing Lens (Fd = 243 mm)

Receiving

             TSI Model 938 Receiving Lens (Fd = 250 mm)

             TSI Model 935 Receiving Lens (Fd = 200 mm)

Photomultiplier

             TSI Model 962 Photomultiplier

Electronics

         TSI Model 985 Bragg Cell Supply and Mixer

         TSI Model 965 Photomultiplier Power Supply

         Tektronix Model 7613 Oscilloscope

         Dantec Model 55L90a Lda Counter Processor

         Tatung TCS-7000 AT computer

# APPENDIX C

## SOFTWARE DESCRIPTION

Data was processed using the Dantec LDA2D software
which allowed variation of the following parameters.

Number of Samples :        2000

Maximum Sampling Time :    30 sec.

Frequency Shift Added :    depended on the flow

Maximum Velocity :         depended on the flow (provided
a                          software filter to reject out of
range data)

Minimum Velocity :         as above

Wavelength :               632.8 nm

Counter Mode :             1 : Fixed Nf

Number of LDA's :          1

Coincidence Filter :       not applicable

First Input Connector :    n/a

Beam Separation :          50 mm

Focal Length :             243 mm

Profile Mode :             n/a

Graphic Adapter :          1 : Hercules

Average data transfer rate @ 7.16 MHz Tatung : 90 kHz

The software compiled the first four moments of the data as well as the mean velocity, rms value, skewness, and flatness.

APPENDIX D


ERROR ANALYSIS


There are two possible sources of error in any LDA based system.  They are optical errors or errors based on the laser and associated optics and electronic errors associated with the signal conversion to usable data.

Errors associated with the optical system can arise from the wavelength $\lambda$ , the beam crossing angle $\phi$, and the frequency shift f.  The wavelength of the light is a fixed value based on energy states in the laser plasma tube and therefore has an insignificant error.

Similarly, the beam crossing angle $\phi$ is a function of the beam separation distance and the focal length and is calibrated at the point of manufacture.

The frequency shift of the light is dependant on the Bragg cell electronics which have an accuracy in the order of 0.1 % [31].

Errors can arise due to the nature of the interference pattern set up by the two beams.  When the two beams are focussed at the measuring volume they produce a Gaussian shaped distribution of frequencies centred on the true frequency.  This is caused by light

scattering and is a source of Doppler broadening errors. Possible broadening errors are gradient broadening, finite transit time broadening, and electronic noise broadening. In turbulence measurements this broadening may be seen by the instrumentation as local velocity fluctuations for some LDA configurations. Using the dual beam interference method with zero crossing detections as in this study the system is insensitive to these errors. As well with the use of the counter a particle must validate both 5 and 8 fringe crossings in the "dual-counter" validation system which eliminates noise to some extent.

Gradient broadening errors occur due to a measurement taken within a volume containing a velocity gradient. Within the measuring volume with a velocity gradient one particle at a lower velocity and another of a higher velocity may be interpreted as velocity fluctuations with time as opposed to spatial variations. This error is estimated to be [32]

$$\left[ \frac{e}{E} \right]_g = \frac{\partial u}{\partial x} \frac{\sigma_x}{u} \qquad \sigma_x - \text{width of measurement volume}$$

For the worst case this was found to be

$$\left[ \frac{e}{E} \right]_g = 0.00183$$

Finite transit time broadening occurs due to the

random arrival and departure of particles in the measurement volume causing fluctuations in phase and therefore frequency. This error is estimated to be

$$\left[\frac{e}{E}\right]_f = \frac{\sqrt{2}}{\pi N_2} \qquad N_2 - \text{number of fringes in measurement volume}$$

For all cases this was found to be

$$\left[\frac{e}{E}\right]_f = 0.00395$$

Electronic noise broadening occurs due to electronic noise in the counter circuitry and in this case was estimated to be less than 1 %.

Errors may arise from velocity biasing which will occur when more particles are carried through the flow at high velocities than at low velocities. If the signal processor accepts all the incoming signals the average of this data will be higher than the true mean velocity. Stevenson, Thompson, and Craig [33] have examined this problem and the effect can be overcome by the use of equal time interval sampling although there is little difficulty in flows where the turbulent intensity is less than 20 %. Highly turbulent flows require careful data collection and there seems to be some controversy regarding the effects of biasing in data collection [34].

Other possible sources of error are listed below. Position errors - Errors associated in locating the

measurement volume at the grid location desired.  As the test section was large compared to the measurement volume the error is estimated to be negligible.

Thus the total error is estimated to be of the order of 2%.

## REFERENCES

1.  Bird, R.B. et al (1960) <u>Transport Phenomena</u>. John Wiley, New York.

2.  as cited in
    Bennett, C.O., <u>Momentum, Heat, and Mass Transfer</u>, McGraw Hill Chem. Eng. Series.

3.  cited in
    Launder, B.E., Spalding, D.B., <u>Lectures in Mathematical Models of Turbulence</u>, Academic Press, London, 1972.

4.  Tennekes, H. and Lumley, J.L., <u>A First Course in Turbulence</u>, MIT Press, Cambridge, Massachusetts, 1972.

5.  Kolmogorov, A.N., (1942) "Equations of turbulent motion of an incompressible turbulent fluid". Izv. Akad. Nauk SSSR Ser. Phy. VI, No.1-2, 56. as cited in [6].

6.  cited in
    Kollman, W. (ed.) <u>Prediction Methods for Turbulent Flows</u>, Hemisphere Pub., Washington, 1980.

7.  Launder, B. and Spalding, D. "The Numerical computation of Turbulent Flows". COmputer Methods in Applied Mechanics and Engineering. 3. 1974.

8.  Launder, B.E., Spalding, D.B., <u>Lectures in Mathematical Models of Turbulence</u>, Academic Press, London, 1972.

9.  Chou, P.Y., (1945) "On the velocity correlations and the solution of the equations of turbulent fluctuation". Quart. Appl. Math. <u>3</u>, 38.

10. Stanisic, M.M. <u>The Mathematical Theory of Turbulence</u>, Springer-Verlag, New York, 1985.

11. Baron, J., Benque, J.P., Coeffe, Y.: "Turbulent Flow Induced by a Jet in a Cavity - Measurements and 3D Numerical Simulation " <u>Turbulent Shear Flows</u>, Springer-Verlag, 1981.

12. Tanaka, N., Moriya, S., Katano, N., Maruoka, H., Wada, A., Fujimoto, K. "Thermal-hydraulic Characteristics in LMFBR Hot Plenum" Civil Engineering Laboratory, Central Research Institute of Electric Power Industry (CRIEPI).

13. Ushijima, S., Kato, M., Fujimoto, K., and Moriya, S. (1987) "Numerical Analyses of Two Dimensional Circulation FLows with a k-e Model and Two Reynolds Stress Models". CRIEPI Report: E385002

14. Boyle, D.R., Golay, M.W., "Measurement of a Recirculating, Two-dimensional, Turbulent Flow and Comparison to Turbulence Model Predictions I: Steady State Case" ASME Paper No. 83-WA/FE-8.

15. Boyle, D.R., Golay, M.W., "Measurement of a Recirculating, Two-dimensional, Turbulent Flow and Comparison to Turbulence Model Predictions II: Transient Case" ASME Paper No. 83-WA/FE-9.

16. Stevenson, W.H., Thompson, H.D., Craig, R.R., "Laser Velocimeter Measurements in Highly Turbulent Recirculating Flows", Journal of Fluids Engineering, 106 No.2, pp. 173-180.

17. Moss, W.D., Baker, S., Bradbury, L.J.S., "Measurements of Mean Velocity and Reynolds Stresses in Some Regions of Recirculating Flow." Turbulent Shear Flows I, Springer-Verlag, 1977.

18. Durst, F., Rastogi, A.K., "Theoretical and Experimental Investigations of Turbulent Flows with Separation," Turbulent Shear Flows I Springer-Verlag, 1977.

19. Smyth, R. "Turbulent Flow Over a Plane Symmetric Sudden Expansion," Journal of Fluids Engineering, 101 pp. 348-353 1979.

20. Schlicting, H. p 750 Boundary-Layer Theory McGraw-Hill, Toronto 1979.

21. Glauert, M.B. "The Wall Jet," Journal of Fluid Mechanics, 1, pp. 625-643 1956.

22. Kruka, V. and Eskinazi, S., "The Wall Jet in a Moving Stream," Journal of Fluid Mechanics, 20 pp. 555-579 1964.

23. Swamy, N.V.C., and Bandyopadhyay, P., "Mean and Turbulence Characteristics of Three-dimensional Wall Jets," Journal of Fluid Mechanics, 71 pp. 541-562 1975.

24. as cited in Schlicting, H. p 750 Boundary-Layer Theory McGraw-Hill, Toronto 1979.

25. Merzkirch, W. Flow Visualization. Academic Press (1974)

26. Porcar, R., Prenel, J.P., "Visualization by means of coherent light sheets: application to different flows." Optics and Laser Technology , October 1982, pp. 261-268

27.  Patankar, S.V., <u>Numerical Heat Transfer and Fluid Flow</u>, Hemisphere, 1980.

28.  Ahluwalia, A.K. and Shoukri, M., "Numerical Simulation of Transient Turbulent Buoyant Flow: The Computer Code FONS TURB"., Ontario Hydro Research Division Report No 82-432-K 1982.

29.  Launder, B.E. and Spalding, D.B., <u>Mathematical Models of Turbulence</u>, Academic, New York 1972.

30.  Swamy, N.V.C., and Bandyopadhyay, P., "Mean and Turbulence Characteristics of Three-dimensional Wall Jets," Journal of Fluid Mechanics, 71 pp. 541-562 1975.

31.  Elphick, I.G. <u>Measurement of Flow Velocities in a Heat Exchanger Model Using LDA</u>, M.A.Sc. Thesis, Dept. Mech. Eng., University of Toronto, 1981

32.  Boyle, D.R., Golay, M.W., "Measurement of a Recirculating, Two-dimensional, Turbulent Flow and Comparison to Turbulence Model Predictions I: Steady State Case" ASME Paper No. 83-WA/FE-8.

33.  Stevenson, W.H., Thompson, H.D., Craig, R.R., "Laser Velocimeter Measurements in Highly Turbulent Recirculating Flows" Journal of Fluids Engineering <u>106</u> June 1984 p 173.

34.  Gouesbet, G., A Review on Measurements of Particle Velocities and Diameters by Laser Techniques, with Emphasis on Thermal Plasmas. Plasma Chemistry and Plasma Processing <u>5</u> 1985 p. 91